**Andreas Hirzer, BSc**

# Physics and Photophysics of the Organic Semiconductor Rubicene

## MASTER THESIS

For obtaining the academic degree
Diplom-Ingenieur

Master Programme of
Technical Physics

**TU Graz**
Graz University of Technology

**Graz University of Technology**

Supervisor:

Univ.-Prof. Dipl.-Ing. Dr.techn. Günther Leising

Institute of Solid State Physics

Graz, August 2010

# Abstract

Over the past few decades organic materials have become promising candidates for various applications in electronics and optoelectronics. Due to the fact that these materials can be processed on a variety of substrates and at low temperatures, they are potential alternatives to inorganic materials used in conventional devices. The fast progress in this field of research gives rise to new applicabilities. Lately solid state organic lasers have gained much interest. Whereas optically pumped solid state organic lasers were successfully demonstrated, electrically driven ones haven't yet been realized. Beside particular laser designs research concentrates on appropriate organic materials which can be used as laser gain mediums. The focus of this master thesis is on rubicene, a poorly investigated organic semiconductor with encouraging properties, and how far rubicene is applicable for solid state organic lasers. Within the scope of this thesis rubicene single crystals are presented, which are obtained from commercially available rubicene powder via the growth from solutions. These crystals are investigated applying different methods. Scanning Electron Microscopy (SEM) and Atomic Force Microscopy (AFM) are used to examine the surface topography of the grown crystals. Additionally the rubicene crystals' chemical composition is revealed through Energy Dispersive X-ray Spectroscopy (EDXS) and by means of Fourier Transform Infrared (FTIR) spectroscopy their chemical purity is determined. Moreover the results of X-ray diffraction (XRD) measurements provide crucial information on the structure of the grown crystals and expose the packing of the molecules within a rubicene crystal. In terms of spectroscopy with visible light the electronic structures of rubicene molecules in solution and of rubicene crystals are investigated. It appears that the grown crystals are chemically very pure and that their surfaces are quite smooth, resulting in a possible application of rubicene crystals as optical resonators in solid state organic lasers. Since the formation of homogeneous organic films is of vital importance for the development of nearly all types of novel organic devices, the growth of rubicene films as well as films of an organic dye, namely a perylene-derivative, from solution on different substrates is examined.

**Keywords:** solid state organic laser, rubicene, crystal growth, optical resonator

# Acknowledgments

# Contents

# List of Figures

# List of Tables

# 1 Introduction

## 1.1 Motivation

Organic materials have been drawing increasing attention because of their interesting optoelectronic properties, which, for instance, manifest in electrically driven luminescence or photovoltaics. Due to their attracting properties these materials are the subject of current research and are already used commercially in a variety of applications. Beside the capability to prepare organic materials on various substrates their favorable processing at room temperature is another great advantage. Nowadays organic field effect transistors (OFETs) represent an intensely investigated application prospect of organic materials. Another very prominent organic device is the organic light emitting diode (OLED), which is already used in consumer electronics. Recently the research topic of solid state organic lasers has attracted attention too. Such lasers would provide a convenient alternative to conventional laser diodes consisting of inorganic semiconductor materials and offer a wide choice of wavelengths for the emission light. In contrast to common liquid dye lasers solid state organic lasers can also be designed to form very compact systems and thus being highly versatile.

The application of organic materials in solid state lasers is topically reviewed by Kranzelbinder et al. [10]. They demonstrate lasing of organic materials in different optically pumped laser designs, such as microcavities, distributed feedback (DFB) structures or ring microlasers and also give an outlook on electrically driven organic lasers. In the following various approaches for solid state organic lasers are presented.

Chen et al. [2] state an optically pumped polymer laser using a circular grating DFB structure which is fabricated by nanoimprint lithography of the laser gain medium. The gain medium is accomplished as thin film which consists of the organic dye rhodamine 640 hosted within a poly(methylmethacrylate) (PMMA) matrix. Lasing occurs as the polymer laser is pumped with laser pulses from a neodymium-doped yttrium aluminum garnet (Nd:YAG) laser. Such optically pumped solid state organic DFB lasers are also demonstrated by Lu et al. [14] and Yamashita et al. [25]. Lasing from a polymer based device is described by Yang et al.

[27]. In this hybrid optoelectronic approach the laser gain medium, a fluorene co-polymer thin film, is optically pumped by a pulsed high-power indium gallium nitride light emitting diode (LED) whose emission light matches with the gain medium's absorption range. For lasing corrugated fused silica is used to achieve a periodically structured gain medium which acts as DFB resonator. Karnutsch et al. [9] as well as Sakata et al. [17] also present very compact solid state organic DFB laser systems which are pumped by an inorganic laser diode and an inorganic LED, respectively. Furthermore Wei et al. [20] even show a solid state organic laser device which, in contrast to the hybrid systems mentioned above, is excited by an OLED. Although the OLED's power density is far too small to reach the lasing thresholds of the organic materials investigated, they expect pulsed high-luminance ultraviolet OLEDs to be able to pump organic films with low lasing thresholds. Another quite interesting approach to obtain solid state organic lasers is introduced by Yamashita et al. [26]. They demonstrate a self-written active waveguide with an in-line Fabry-Pérot cavity. The waveguide is fabricated through photopolymerization of a resin doped with organic dye molecules in the gap between two aligned optical fibers. Additionally two half-mirrors are placed in the resin to form an optical feedback cavity of the Fabry-Pérot type. Since this device is directly prepared between two optical fibers it can be automatically interconnected with input and output units. As the organic dye in the self-written active waveguide is optically pumped by a dye laser (dye: Nile Blue 690) lasing can be observed in the emission spectrum of this solid state organic laser, which is practically measured via one of the optical fibers.

Besides solid state lasers where the gain medium is carried out as thin organic film or as layer doped with an organic dye organic single crystals are promising candidates for solid state lasers too. Yamao et al. [24] verify longitudinal multimode laser oscillations in an organic single crystal of a thiophene/phenylene co-oligomer as it is optically pumped with light pulses provided from an optical parametric oscillator together with a Nd:YAG-laser. The laser oscillations, which are observed from pairs of parallel crystal facets, indicate that the single crystal acts as Fabry-Pérot resonator of high reflectivity due to the parallel facets and the crystal's high refractive index of 4.0. In a similar experiment Xie et al. [23] also demonstrate the emission of laser light from a high-quality distyrylbenzene derivative crystal. These remarkable results mean that solid state organic lasers can be realized from organic single crystals of acceptable quality without the need for fabricating elaborately structured DFB resonators since the crystals themselves act as optical resonators. A description of various growth methods to obtain regular high-quality crystals, such as vapor- and solution-processed techniques, is presented by Li et al. [13].

The huge potential which is attributed to solid state organic lasers is reflected by the extensive efforts in research concerning these innovative laser devices. As a consequence
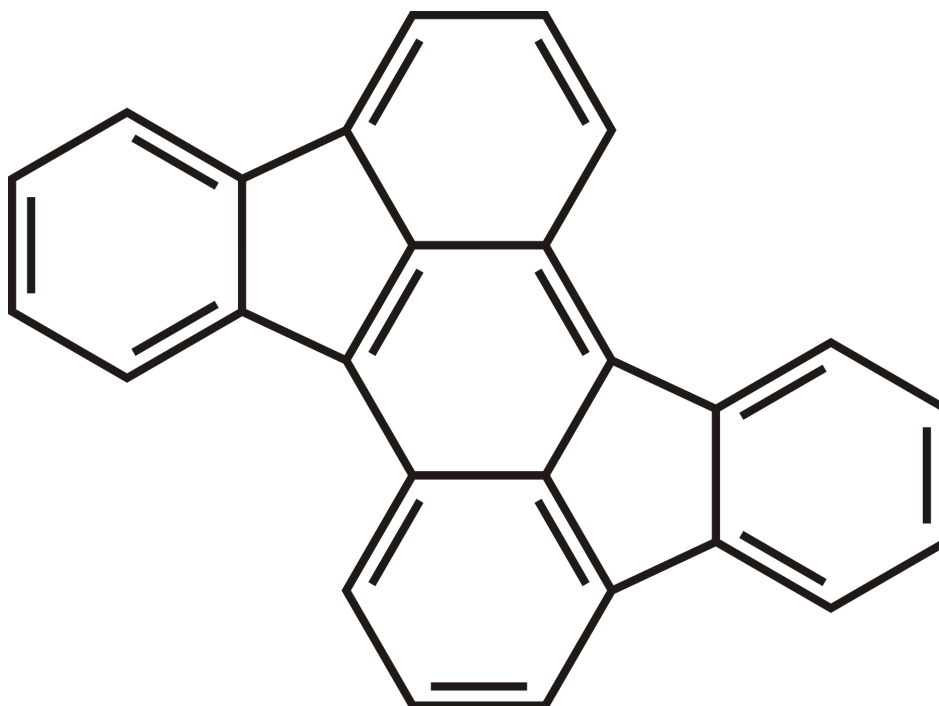
**Figure 1.1:** Molecular structure of rubicene ($C_{26}H_{14}$).

many different organic materials are being inspected in order to use them in solid state organic lasers. The organic material investigated within the scope of this master thesis is rubicene, particularly with regard to its physical properties, such as the structure of rubicene crystals and the packing of the molecules in these crystals, and its photophysical properties, which are characterized by the fact that the absorption range of rubicene covers the wavelength of light emitted from a frequency-doubled Nd:YAG-laser, allowing for straightforward excitation with laser light.

## 1.2 Rubicene

So far rubicene is a poorly investigated organic semiconductor, although its optoelectronic properties seem to be very promising. A single rubicene molecule is planar and consists of 26 carbon atoms and 14 hydrogen atoms. From the molecule's structure, depicted in Figure 1.1, one can see that rubicene is a polycyclic aromatic hydrocarbon which is constructed of linked aromatic rings. The molar mass of rubicene is 326.4 g/mol and it melts at a temperature of 305 °C, according to the data of Acros Organics (Geel, Belgium), the supplier from which the rubicene used in this thesis is obtained.

## 1.3 Outline of the Master Thesis

In the beginning some fundamental aspects are outlined in Chapter 2. In Section 2.1 the basic principles regarding the description of crystals and their structures are mentioned. Furthermore a quantum-mechanical explanation of the optical absorption process, which is essential for many investigations within the field of spectroscopy, is given in Section 2.2.

Chapter 3 describes the experimental part of the thesis. Section 3.1 is devoted to the growth of rubicene crystals from solutions. In the following the grown crystals are examined with respect to their surface topography and chemical composition (see Section 3.2). Moreover the structure of the grown rubicene crystals is revealed in Section 3.3. Rubicene is spectroscopically investigated too, both molecules in solution (see Section 3.4) and in solid state (see Section 3.5). Finally Section 3.6 shows some qualitative results of growth experiments of rubicene and of an organic dye, namely a special perylene-derivative, on the surfaces of several substrates.

In Chapter 4 an outlook of possible applications of rubicene single crystals in future is given. Thereby the focus is on the crystals' capability to be used as solid state organic laser and, more specifically, how far a rubicene single crystal is suitable to be applied as optical resonator (see Section 4.1).

To conclude Chapter 5 contains a brief summary of the most important results achieved during this master thesis.

# 2 Fundamentals

## 2.1 Crystals

This section follows the remarks in [21]. Crystals are built up of regularly arranged atomic elements. Due to this periodicity any crystal can be defined by its specific structure. To describe the periodic crystal structure a spatial lattice of equivalent points is introduced. The corresponding crystal structure is only obtained if every lattice point is replaced by the same basis, which might consist of atoms, ions, atom groups or molecules, depending on the type of crystal. However just an ideal, infinitely expanded crystal can be characterized by such a lattice. In case of real crystals disorders occur in the form of surfaces and numerous structural defects within the bulk and thus real crystals can't comply with the strict periodicity of a crystal lattice. Consequently the following remarks solely count for ideal crystals.

### 2.1.1 Crystal Lattice

Since all lattice points in a crystal lattice are equivalent, the whole lattice can be constructed by translation operations along three directions in space, beginning with a starting point $\mathbf{R}_0$. Then the position of any lattice point is determined by a certain lattice vector $\mathbf{R}$:

$$\mathbf{R} = \mathbf{R}_0 + n_1\mathbf{a}_1 + n_2\mathbf{a}_2 + n_3\mathbf{a}_3, \tag{2.1}$$

where $n_1$, $n_2$ and $n_3$ are integers and $\mathbf{a}_1$, $\mathbf{a}_2$ and $\mathbf{a}_3$ are the non-planar basis vectors of the lattice, which are directed from $\mathbf{R}_0$ to the next lattice points in all three three directions in space. Their absolute values are called lattice parameters. Moreover these lattice basic vectors span a parallelepiped which is called unit cell. It's obvious that stringing together the unit cells completely yields the crystal. Although the crystal lattice is clearly defined by a set of lattice basic vectors, contrariwise different lattice basic vectors, respectively unit cells, can be allocated to the same crystal lattice. Among these the smallest possible ones are called primitive. Accordingly a primitive unit cell only contains one lattice point. In this special

case the corresponding crystal lattice is called Bravais lattice. For a three-dimensional space there are 14 of these primitive lattices.

Symmetry operations are operations which leave the crystal lattice invariant since they only transfer lattice points into other, equivalent lattice points. Besides the already mentioned general translation operations

$$\mathbf{T} = n_1\mathbf{a}_1 + n_2\mathbf{a}_2 + n_3\mathbf{a}_3, \qquad (2.2)$$

which define the crystal lattice, there are various other symmetry operations based on rotations, reflections and inversions. In addition to it such non-translational symmetry operations can be combined in various ways. Any combination which leave the crystal lattice invariant represents a so called point group. Considering just translation operations (Equation 2.2) the number of possibilities to define a crystal lattice by its unit cell is infinite. A clear classification can be achieved with aid of the additional non-translational symmetry operations that leave the crystal lattice invariant. In case of three-dimensional primitive lattices all together 7 distinct point groups exist. Primitive crystal lattices can now be distinguished according to these point groups, resulting in 7 different crystal systems. Furthermore a combination of the symmetry operations specified by the point groups with translation operations leads to so called space groups. Consequently a space group contains all symmetry operations which leave the crystal lattice invariant. For primitive crystal lattices 14 space groups occur, whereby each of them is attributed to one of the 14 Bravais lattices. Table 2.1 lists all Bravais lattices of each crystal system. A precise description of the Bravais lattices and the geometrical properties of their unit cells can be found in [21].

The crystal structure is obtained if every lattice point is occupied by the same basis. If this basis is spherically symmetric with respect to its lattice point one gets the same 7 point groups that define the crystal systems. But in general the basis can't be regarded as spherically symmetric with respect to its lattice point and thus additional point groups occur in each crystal system. Due to the reduced symmetry these point groups contain less elements than the ones in case of spherical symmetry of the basis. Considering all crystal systems there are a total of 32 different point groups which correspond to an equal number of crystal classes. This great amount of point groups yields not less than 230 possible space groups for a crystal.

An extension of the lattice basis vectors forms the axes of a specific coordinate system, which allows a specification of certain points, directions and planes within the crystal lattice. Conveniently the zero point is placed at the position of a lattice point. In doing so a lattice point is simply characterized by the integer coefficients of its lattice vector. A certain direction

**Table 2.1:** Crystal systems and corresponding Bravais lattices.

| Crystal system | Bravais lattice |
|---|---|
| Triclinic | Primitive triclinic |
| Monoclinic | Primitive monoclinic |
| | Base-centered monoclinic |
| Orthorhombic | Primitive orthorhombic |
| | Base-centered orthorhombic |
| | Body-centered orthorhombic |
| | Face-centered orthorhombic |
| Tetragonal | Primitive tetragonal |
| | Body-centered tetragonal |
| Trigonal | Primitive trigonal |
| Hexagonal | Primitive hexagonal |
| Cubic | Primitive cubic |
| | Body-centered cubic |
| | Face-centered cubic |

in the lattice is determined by the smallest integer coefficients of the lattice vector along this direction. Lattice planes are described via their intersections with the axes of the coordinate system, expressed in terms of integer multiples of the three lattice parameters. For description the reciprocals of these integer multiples are determined and then the smallest triple of integers with the same ratio is built. The obtained integers are used to designate lattice planes and called Miller indices $(hkl)$.

### 2.1.2 Reciprocal Lattice

For every crystal lattice, generated by particular translation operations 2.2, it's possible to construct a reciprocal lattice. Any vector $\mathbf{G}$ which connects two points of the reciprocal lattice is defined analogous to a lattice vector in real space:

$$\mathbf{G} = m_1\mathbf{b}_1 + m_2\mathbf{b}_2 + m_3\mathbf{b}_3, \tag{2.3}$$

where $m_1$, $m_2$ and $m_3$ are integers and $\mathbf{b}_1$, $\mathbf{b}_2$ and $\mathbf{b}_3$ are the basis vectors of the reciprocal lattice. These can be calculated from the basic vectors of the crystal lattice in real space, according to:

$$\mathbf{b}_i = 2\pi\frac{\mathbf{a}_j \times \mathbf{a}_k}{\mathbf{a}_i(\mathbf{a}_j \times \mathbf{a}_k)} \tag{2.4}$$

Furthermore the basic vectors of both lattice systems are related to each other in the following way:

$$\mathbf{a}_i \mathbf{b}_j = 2\pi \delta_{ij} \tag{2.5}$$

This means that the coordinate systems of the crystal lattice in real space and the reciprocal lattice, which are spanned by the respective set of basic vectors, are orthogonal to each other. As a result the reciprocal lattice vectors are perpendicular to certain lattice planes in real space and vice versa.

The reciprocal lattice plays a mayor role in diffraction analyses of crystal structures since the reflections of constructively interfering beams, e.g. X-rays, directly correspond to the points of the reciprocal lattice. That implies that crystal structures can be identified from their diffraction patterns.

## 2.2 Optical Absorption

In the process of optical absorption a photon of certain energy is dissipated as it impinges on an atom, molecule or solid. Thereby the photon's energy is transferred to an electron which subsequently is excited into an energetically higher state, according to the electron's energy gain. A quantum mechanical description of the optical absorption process can be achieved in the course of time-dependent perturbation theory. The following section is deduced from [3, 5, 11].

### 2.2.1 Transition Probability of Electrons

The absorption process is governed by the system's probability for a transition from an initial to a final electronic state. In terms of optical absorption the initial state is usually the ground state, whereas the final state is an excited state. The determination of the transition probability is a problem which is quantum-mechanically treated within perturbation theory, where an electromagnetic wave acts as time-dependent perturbation of the system. Therefore the Hamiltonian $\hat{H}$ is split into a time-independent part $\hat{H}_0$ and a time-dependent perturbation $\hat{H}_1(t)$, which is assumed to be small compared to the energy of the system:

$$\hat{H}(t) = \hat{H}_0 + \hat{H}_1(t) \tag{2.6}$$

The time-dependent Schrödinger equation of the disturbed system reads:

$$i\hbar\frac{\partial}{\partial t}\Psi(\mathbf{r},t) = [\hat{H}_0 + \hat{H}_1(t)]\Psi(\mathbf{r},t) \tag{2.7}$$

Time evolution of the stationary wave functions $\Phi_n(\mathbf{r})$, which are determined by the time-independent Schrödinger equation of the undisturbed system,

$$\hat{H}_0\Phi_n(\mathbf{r}) = E_n\Phi_n(\mathbf{r}), \tag{2.8}$$

results in:

$$\Phi_n(\mathbf{r},t) = \Phi_n(\mathbf{r})e^{-\frac{i}{\hbar}E_n t} \tag{2.9}$$

Thereby the energies $E_n$ are the eigenvalues of the undisturbed system. Moreover the wave functions 2.9 are solutions of the time-dependent Schrödinger equation of the undisturbed system. A linear combination of them is used as ansatz for the solution of the time-dependent Schrödinger equation of the disturbed system 2.7:

$$\Psi(\mathbf{r},t) = \sum_n a_n(t)\Phi_n(\mathbf{r},t) \tag{2.10}$$

It should be mentioned that the coefficients $a_n$ have to be explicitly time-dependent since the time-dependence of the wave functions $\Phi_n(\mathbf{r},t)$ only concerns the undisturbed system. Inserting this ansatz into Equation 2.7 leads to:

$$i\hbar\sum_n\frac{da_n(t)}{dt}\Phi_n(\mathbf{r})e^{-\frac{i}{\hbar}E_n t} = \sum_n a_n(t)\hat{H}_1(t)\Phi_n(\mathbf{r})e^{-\frac{i}{\hbar}E_n t} \tag{2.11}$$

Multiplication from the left with $\Phi_f^*(\mathbf{r},t)$, subsequent integration over space and taking into account orthogonality finally yields the following set of coupled differential equations for the time-dependent coefficients:

$$\frac{da_f(t)}{dt} = -\frac{i}{\hbar}\sum_n a_n(t)H_{1,\,fn}(t)e^{\frac{i}{\hbar}(E_f-E_n)t}, \tag{2.12}$$

with the matrix elements

$$H_{1,\,fn}(t) = \langle\Phi_f|\,\hat{H}_1(t)\,|\Phi_n\rangle \tag{2.13}$$

On the assumption that the undisturbed system is in an initial state $\Phi_i$ before the perturbation begins to influence the system at the time $t = 0$, one obtains the following relations, according to Equations 2.9 and 2.10 and the normalization condition for $\Psi(\mathbf{r},t)$:

$$a_i(0) = 1 \quad\text{and}\quad a_n(0) = 0 \quad \forall\, n \neq i \tag{2.14}$$

In the case of a small perturbation these relations are also a reasonable approximation for the coefficients at any times $t > 0$:

$$a_i(t) \approx 1 \qquad \text{and} \qquad a_n(t) \approx 0 \quad \forall \ n \neq i \tag{2.15}$$

Applying these simplification the coupled differential equations 2.12 become:

$$a_f(t) = -\frac{i}{\hbar} \int_0^t H_{1,\ fi}(\tau) e^{i\omega_{fi}\tau} d\tau, \tag{2.16}$$

with the transition or resonance frequency

$$\omega_{fi} = \frac{E_f - E_i}{\hbar}, \qquad \text{with } E_f > E_i \tag{2.17}$$

The probability of the originally undisturbed system to change from an initial electronic state $\Phi_i$ to a final electronic state $\Phi_f$ at a certain time $t$ after the onset of the perturbation is determined by the square of the absolute value of the corresponding coefficient:

$$P_{fi}(t) = |\langle \Phi_f | \Psi(t) \rangle|^2 = |a_f(t)|^2 \tag{2.18}$$

In the process of optical absorption the perturbation is periodic since it is caused by the interaction of the electrons with the incoming light's electromagnetic wave of angular frequency $\omega$:

$$\hat{H}_1(t) = \hat{H}_1 \cos(\omega t) \tag{2.19}$$

Inserting this perturbation into Equation 2.16 and taking into account Equation 2.18 result in the following transition probability in case of optical absorption:

$$P_{fi}(t) = |H_{1,\ fi}|^2 \frac{\sin^2[\frac{t}{2}(\omega_{fi} - \omega)]}{\hbar^2 (\omega_{fi} - \omega)^2} \tag{2.20}$$

From the equation above one can clearly see that the transition probability has maxima only for certain times $t$ and that a transition from an initial to a final electronic state most likely happens if the periodicity of the perturbation matches the resonance frequency. Finally it should be pointed out that the derivated transition probability is a general expression for any type of optical absorption.

# 3 Experimental

## 3.1 Growth of Rubicene Crystals from Solutions

The growth of organic crystals of high crystallographic quality and chemical purity is an attractive field of research in solid state physics because of their interesting optical properties, which, for instance, qualify such crystals to be used as optical resonators (see Section 1.1). Moreover the outstanding features of organic crystals give rise to innovative areas of application, especially in micro- and optoelectronics.

As described in [1, 21], there are different manners to grow crystals, such as the Czochralski process where crystals are grown from the melt. This method is used to obtain large single crystals of metals, semiconductors or salts. A very important application of the Czochralski process is the growth of highly pure, cylindrical single crystals made of silicon. Thin slices of these silicon single crystals, so called wafers, serve as substrates for the fabrication of integrated circuits and microelectronic devices and play a major role in semiconductor industry. Crystals can also be grown from the vapor phase. The growth from the vapor phase is essential for materials with very high melting points or for materials which sublime. During this growth process a temperature gradient between a dissolution zone (higher temperature) and a growth zone (lower temperature) causes the chemical transport. This method yields extremely high-quality crystals. Nevertheless one of the most common methods to form organic crystals is the growth from a solution. For crystallization from the liquid state into an ordered solid state the solution has to be supersaturated. This can be achieved in different ways, for instance by slowly cooling the solution or by reduction of the solubility of the solvent. If the solvent is evaporated slowly the solution becomes supersaturated too. The latter is the method chosen within the scope of this thesis. Once the solution becomes supersaturated nucleation is initiated. The formation of nuclei strongly depends upon the presence of impurities as well as on the surfaces of the vessel containing the solution. The nuclei subsequently begin to grow and more and more material crystallizes in the solution. After the evaporation of all the solvent the crystals remain in the vessel. Size and quality of the grown crystals are determined by different factors, e.g. the solubility of the solvent, the number of nucleation

sites, the crystallization time and of course environmental influences, which affect deposition (e.g. external vibrations).

### 3.1.1 Solution Preparation

For preparation of the rubicene solutions rubicene powder, derived from Acros Organics, is used. It has a purity of $98\%$. To obtain saturated solutions the same amount of rubicene powder is dissolved in three organic solvents, namely cyclohexanone ($C_6H_{10}O$, purity: $\geq 99.5\%$), chlorobenzene ($C_6H_5Cl$, purity: $\geq 99\%$) and toluene ($C_7H_8$, purity: $\geq 99.9\%$). Different amounts of powder which are precipitated out of each solution evince disparate solubilities of rubicene in these solvents. Among them cyclohexanone has the poorest rubicene solubility. However the solubility of rubicene is moderate in chlorobenzene and excellent in toluene. Each saturated rubicene solution is mixed in a test tube. For crystal growth the solutions have to be kept in clean growing vessels. Therefore Petri dishes are thoroughly cleaned with isopropyl alcohol ($C_3H_8O$). First approximately $3\,ml$ of each solution are drawn up into syringes. Then each of the solutions in the syringes is poured into a Petri dish, thereby being filterd through a $0.22\,\mu m$ syringe filter in order to avoid infiltration of particles into the growth solutions, which should be as pure as possible. To enable a very slow evaporation rate of the solvents the Petri dishes are finally covered with slightly bigger Petri dishes. For comparison of the grown crystals all three dishes are kept in the same environment at room temperature to allow equal growth conditions for all rubicene solutions.

### 3.1.2 Crystals from a Rubicene-Cyclohexanone Solution

After about 7 days, when all the solvent is evaporated from the rubicene-cyclohexanone solution, the grown rubicene crystals remain in the Petri dish. As shown in Figure 3.1 there are many very small crystals (length in a few tens $\mu m$ range) which are strongly grown together. The bigger agglomerations of crystallized rubicene in between the small rubicene crystals are rather branched. All in all crystal growth from the rubicene-cyclohexanone solution doesn't yield reasonable rubicene single crystals.
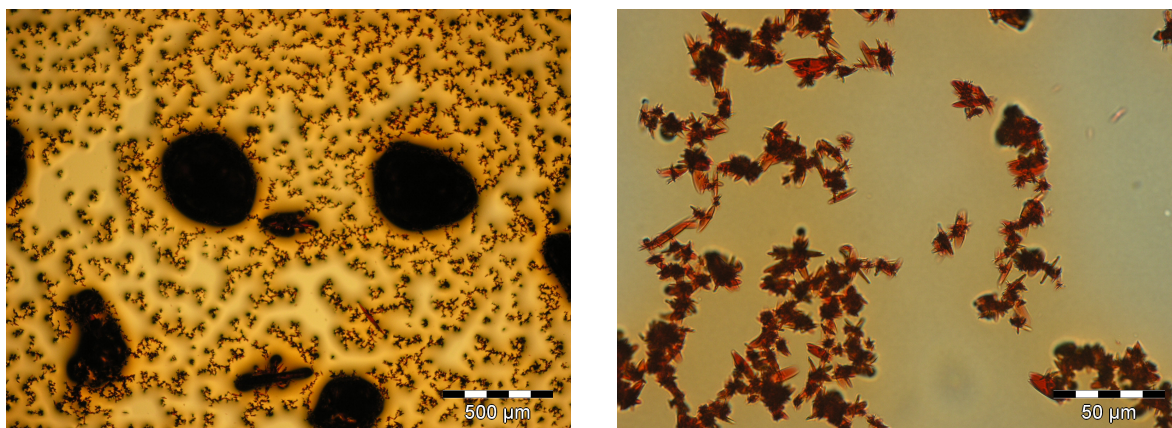
**Figure 3.1:** Crystals grown from the rubicene-cyclohexanone solution. The left image shows a lot of very small rubicene crystals and some bigger agglomerations of crystallized rubicene. In the right image one can see that the formed rubicene crystals are strongly grown together.
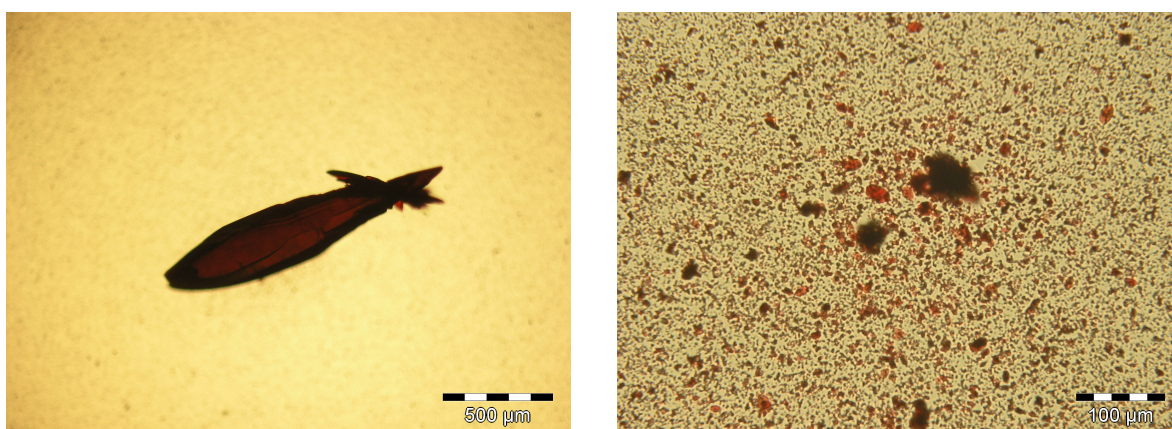


**Figure 3.2:** Crystals grown from the rubicene-chlorobenzene solution. In the left image a larger rubicene crystal of more than $1\,\mathrm{mm}$ length is depicted. On the right agglomerations of crystallized rubicene in between smaller rubicene crystals are shown.

### 3.1.3 Crystals from a Rubicene-Chlorobenzene Solution

After approximately 8 days all the solvent is evaporated from the rubicene-chlorobenzene solution. Figure 3.2 evinces that the rubicene crystals grown from the rubicene-chlorobenzene solution are similar to those grown from the rubicene-cyclohexanone solution. Again the crystals are mainly small, with some bigger, highly branched agglomerations of crystallized rubicene in between them. Furthermore there are some appreciably larger rubicene crystals which have a length in the range of a few mm. Nevertheless these crystals can't be regarded
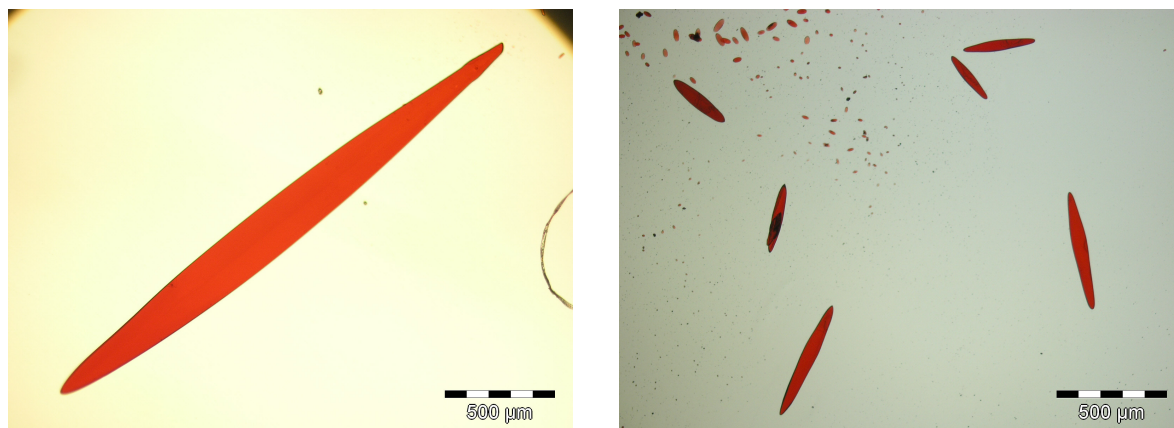
**Figure 3.3:** Crystals grown from the rubicene-toluene solution. The left image shows a very large rubicene crystal of several mm length. In the right image smaller crystals are depicted. All crystals are flat and grown without branches.

as single crystals because of their branched growth.

### 3.1.4 Crystals from a Rubicene-Toluene Solution

The time needed for crystals to grow from the rubicene-toluene solution is about 12 days. On the one hand there are very small crystals with a length in the range of 100 µm and below, on the other hand some of the crystals grow from the rubicene-toluene solution are quite large. The length of these larger crystals ranges from approximately half a mm up to several mm (see Figure 3.3). The rubicene crystals seem to be very flat and have an elongated oval shape with no branches. Thus the crystals grown from the rubicene-toluene solution are expected to be rubicene single crystals of acceptable quality.

According to the results from all three growth experiments the solution of choice for growing rubicene crystals is the rubicene-toluene solution. Hence all further rubicene crystals investigated within the scope of this thesis are grown from a rubicene-toluene solution.

## 3.2 Crystal Surface Topography and Composition

For investigating the surface topography and chemical composition of the grown rubicene crystals various analytical methods are applied. A Scanning Electron Microscope (SEM)

allows a closer look onto the surface topography and is able to reveal fine details of the crystal surface. Supplementary a SEM, in addition operated with a detector for Energy Dispersive X-ray Spectroscopy (EDXS), can identify the chemical composition of the crystal. Compared to a SEM an Atomic Force Microscope (AFM) can acquire images of the structures on the crystal surface with higher resolution. Beside height images of the surface topography an AFM allows the detection of variations in the material properties of the crystal surface. Furthermore Fourier Transform Infrared (FTIR) spectroscopy provides IR spectra which give information on the atomic bonds of the crystal. In this way an evaluation of the crystal's chemical purity is possible.

### 3.2.1 Scanning Electron Microscopy

The basic knowledge of this topic is deduced from [6]. In a SEM an electron beam is used to probe the specimen. To generate the beam electrons are emitted from a thermionic or field-emission cathode and subsequently accelerated towards an anode by a voltage of typically $1\,\text{kV}$ to $50\,\text{kV}$. An electron lens system consisting of several magnetic coils focuses the electron beam onto the target. After the penetration of the specimen the primary electrons are decelerated via a number of elastic and inelastic atomic scattering processes. As a consequence of the gradual electron energy diminution the electron interaction volume within the specimen has a finite range of about $0.1\,\mu\text{m}$ to $10\,\mu\text{m}$, depending on the electron energy and the density of the material. The information depth is approximately half the electrons' penetration depth into the specimen since the electrons have to leave the specimen to get to the detector. For imaging the specimen surface low energy secondary electrons are used. These electrons are extremely susceptible to elastic and inelastic scattering and hence can leave the specimen only from a very thin surface layer of a few nm thickness. Secondary electrons are knocked out of atoms in this thin surface layer not only by the primary electrons entering the layer but also by backscattered electrons from inside the specimen. The topographic contrast of the surface occurs from the dependence of the secondary electron yield on the tilt angle of a surface element and from the enhanced electron emission at tips, edges or small particles. The image is formed by scanning the focused electron beam in a raster pattern over the surface and measuring the number of emitted electrons for each point in the raster pattern. For detection of the secondary electrons usually an Everhart-Thornley detector is used. The whole imaging process proceeds under high vacuum conditions to avoid unpreferred interactions between electrons and atoms or molecules of an ambient air. SEMs can reach a resolution in the range of $1\,\text{nm}$ to $5\,\text{nm}$ depending on the material investigated and the electron energy.

Since most SEMs are equipped with a semiconductor detector for EDXS an elemental
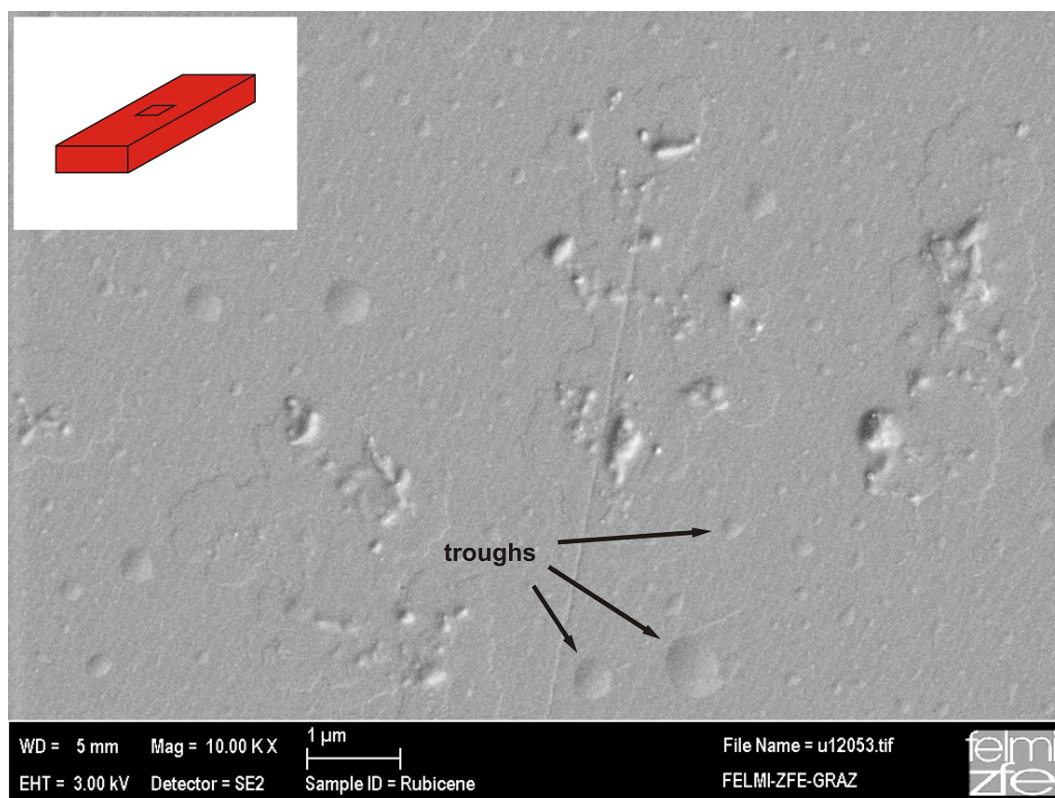
**Figure 3.4:** SEM image of a rubicene crystal's surface. Beside small particles there are remarkably circular troughs all over the surface (some of them are denoted). In the inset, which schematically shows the rubicene crystal, the surface area investigated is indicated.

analysis of the specimen can be done apart from imaging the surface. If electrons pass through the specimen they can ionize atoms by knocking out an electron from an inner shell. Then the so formed hole will be filled by another electron from an outer shell. Thereby the energy difference between outer and inner shell electron is released, either directly via emission of an outer shell electron with some remaining kinetic energy (Auger electron) or alternatively via emission of a X-ray photon. The energy of this photon is characteristic for the atom involved. Hence these X-rays are used for EDXS. From the position of the characteristic X-ray lines in the EDX spectrum one can identify the elements in the specimen (except light elements like hydrogen or helium). The X-ray lines' intensities give information on their concentration.

The SEM measurements were carried out on a Gemini DSM 982, an analytical high resolution SEM manufactured by LEO (Oberkochen, Germany), equipped with a Voyager 3105A EDX detector from Noran Instruments Inc. (Middleton, USA) at the Austrian Centre for Electron Microscopy and Nanoanalysis.
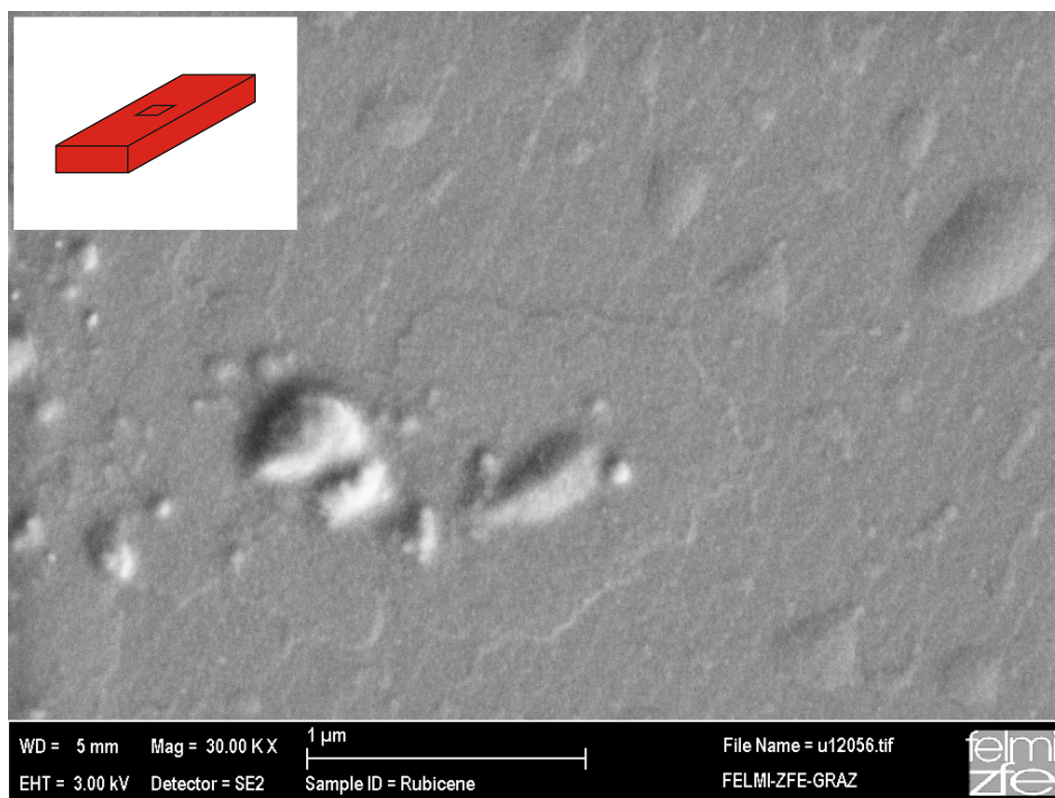
**Figure 3.5:** SEM image of small particles on a rubicene crystal's surface. Moreover the image shows a terrace grown on the surface. The inset schematically indicates the area investigated on the crystal surface.

### 3.2.1.1 Surface Topography

Since rubicene crystals are insulating specimens they have to be coated with a conductive layer for SEM measurements. Otherwise charging can occur and lead to a negative surface potential which acts as a retarding field for the primary electrons. As a consequence the SEM image becomes blurred. To avoid charging effects the rubicene crystal is placed on a conductive carbon cellotape and sputtered with gold and palladium before imaging with the SEM. Figure 3.4 depicts the surface of the crystal. One can notice some small particles, most likely pollutants, on the rather flat surface. Furthermore there are differently large circular troughs which expand over the whole surface of the rubicene crystal. The surface also shows the growth of terraces which is clearly visible in Figure 3.5. Figure 3.6 illustrates the edge of the rubicene crystal. There isn't one sharp edge but rather several steps on the surface towards the edge.
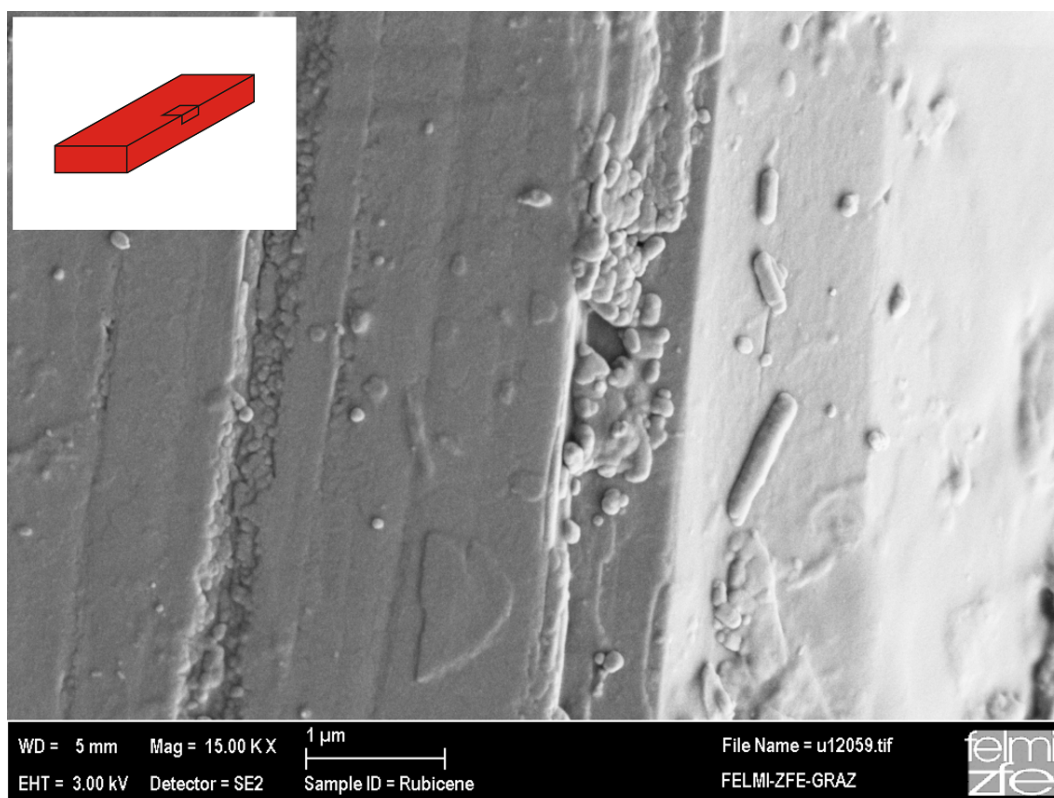
**Figure 3.6:** SEM image of the cascaded edge of a rubicene crystal. The darker area represents the crystal's top surface whereas the brighter area shows the side of the crystal. The inset schematically illustrates the crystal edge investigated.

### 3.2.1.2 Elemental Analysis

For EDXS another rubicene crystal is used. It is placed on a conductive carbon cellotape, just like the crystal used for SEM imaging. But this time the crystal is sputtered with carbon instead of gold and palladium. The EDX spectra depicted in Figure 3.7 give information on the chemical composition of the rubicene crystal. For comparison two spectra are shown, recorded at different crystal positions. Both spectra clearly demonstrate that the rubicene crystal mainly consists of carbon. There are little contaminations with silicon which probably originate from other specimens during storage of the rubicene crystals. The EDX spectrum of the carbon cellotape in Figure 3.8 evinces that the oxygen peaks in both EDX spectra of the crystal are contributions from the cellotape. All EDX spectra are superimposed by continuous spectra which arise from bremsstrahlung generated by the electron's deceleration in matter. Finally it should be pointed out that there is no sulfur present in the grown rubicene crystal, which is a measure of the crystal's high quality. For instance Sachweh et al. [16] mention sulfurous impurities in the rubicene gained from their synthesis. Moreover they state that such impurities strongly hamper crystal growth.
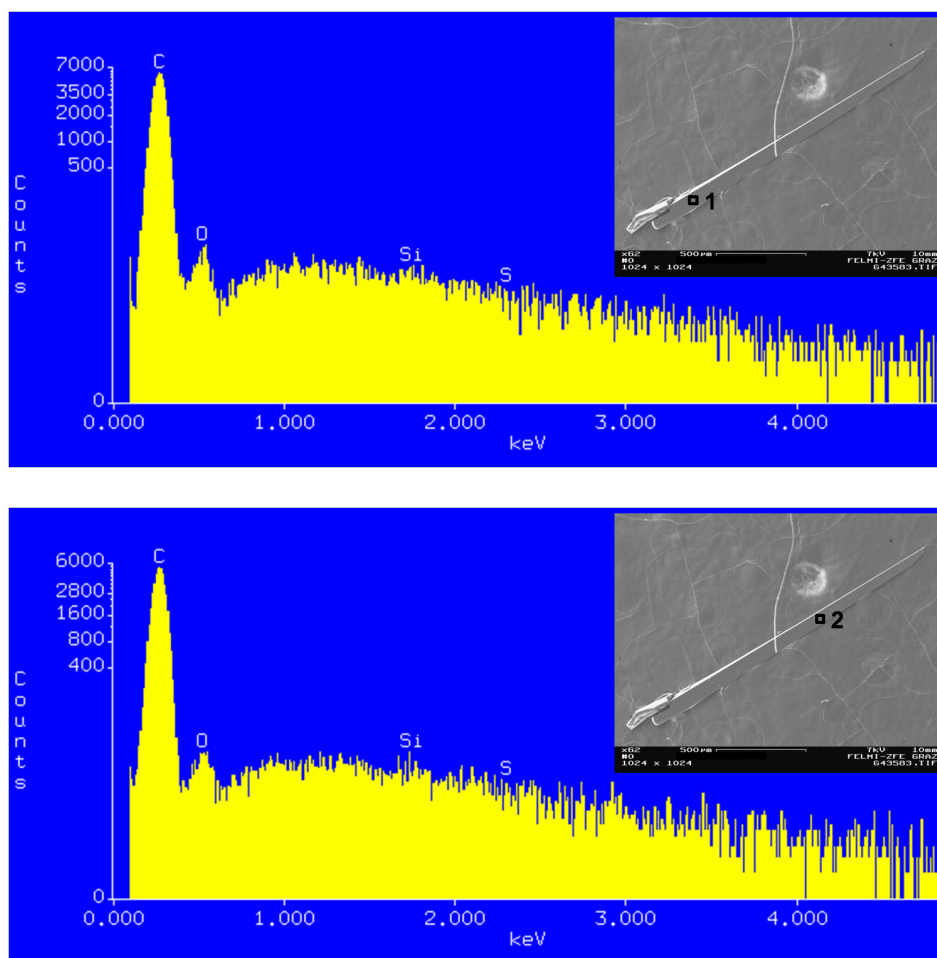
**Figure 3.7:** The EDX spectra reveal the chemical composition at position 1 (upper image) and position 2 (lower image) of the rubicene crystal. The insets show SEM images of the crystal on the carbon cellotape in which these positions are marked.
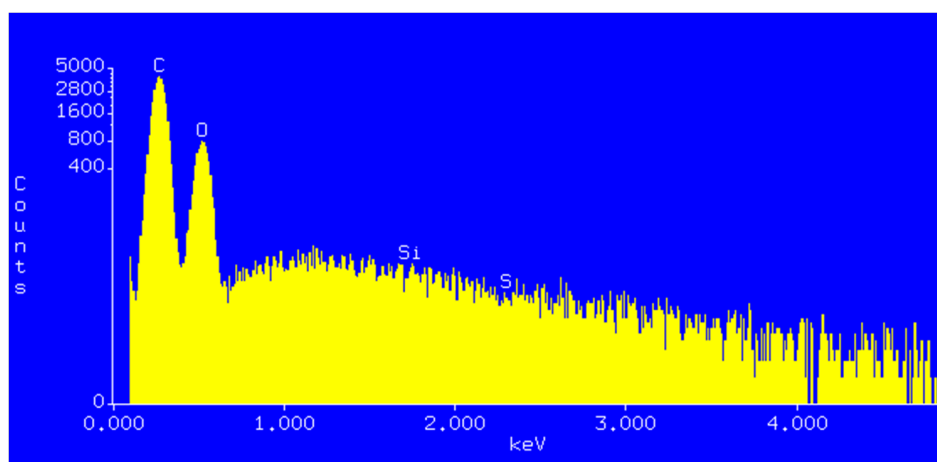


**Figure 3.8:** EDX spectrum of the carbon cellotape.

### 3.2.2 Atomic Force Microscopy

An AFM uses a very fine probe to scan the surface of the specimen. In contrast to the Scanning Tunneling Microscope (STM), which is limited to specimen with conductive surfaces since a tunneling current between the microscope's tip and the specimen is used for imaging, the AFM is capable of investigating insulating surfaces too, making it a powerful tool in the field of organic materials science. The AFM can be operated in different imaging modes. In general the imaging modes are divided into contact mode, non-contact mode and intermittent-contact or tapping mode [19].

**Contact mode:** In this mode the AFM probe, usually a sharp pyramid-shaped tip mounted on a cantilever, makes contact with the specimen surface. A piezo scanner is used to generate a well defined relative motion between probe and surface. During scanning the cantilever is deflected by repulsive forces from height variations of the surface. These deflections are detected via a laser beam reflected from the cantilever's upper side and a position sensitive photodetector which can measure displacements of the incoming laser beam as small as 1 nm. Usually the deflection of the cantilever is kept constant with the aid of a feedback system that signals the piezo scanner to move the specimen up and down. From the piezo scanner's vertical motion a three-dimensional image of the specimen's surface topography can be achieved. Figure 3.9 schematically shows an AFM setup for contact mode imaging.

**Non-contact mode:** In this mode the AMF probe on the cantilever doesn't contact the specimen. Instead the probe is operated about 1 nm to 10 nm above the specimen surface.
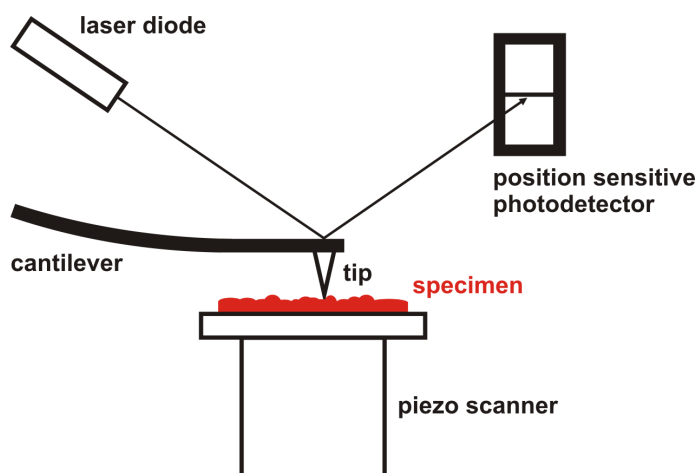


**Figure 3.9:** Schematic setup of an AFM operated in contact mode.

On the one hand the non-contact mode prevents the probe from degradation and on the other hand the specimen surface isn't damaged by the tip. Therefore this mode is advantageous for studying soft specimen. For AFM measurements in non-contact mode the cantilever has to vibrate near its resonance frequency. The resonance frequency varies as the cantilever experiences attractive forces in the proximity of the specimen surface which depend on the distance between tip and surface. The surface topography information is obtained equally to contact mode imaging by a feedback system that moves the piezo scanner up and down in order to keep the resonance frequency constant during scanning. In contrast to contact mode operations the non-contact mode has a disadvantage if there are adsorbed fluid layers on the surface. While an AFM tip in contact mode penetrates the liquid layer and images the underlying surface an AFM tip in non-contact mode oscillates above the liquid layer and images both the specimen surface and the adsorbed fluid layer.

**Intermittent-contact mode:** This mode works similar to the non-contact mode. The cantilever is also driven near its resonance frequency but the probe is brought closer to the specimen surface so that it barely taps the surface during scanning. The intermittent-contact or tapping mode is a very important AFM technique since it reduces the damage done to the AFM probe and the specimen surface compared to contact mode and despite is able to image the surface topography under adsorbed fluid layers on the surface.

The geometry of the AFM probe crucially determines the reachable resolution. Radius and half cone angle of the tip should be as small as possible to avoid adulterated measurements of the surface topography due to the tip's finite extent. For instance a single-walled carbon nanotube would be an excellent AFM probe because of its very small tip radius (in the nm range and below) and its cylindrical structure.

Additionally Phase Detection Microscopy (PDM) can be performed in any imaging mode for which the cantilever is forced to vibrate. Phase images of the specimen surface are acquired from the phase lag between the signal that drives the cantilever to oscillate and the actual cantilever oscillation. Changes in the phase lag reflect variations in the mechanical properties of the specimen surface such as elasticity, adhesion or surface tension.

The AFM measurements were carried out on a Dimension 3100 Scanning Probe Microscope (SPM) from Veeco Instruments Inc. (New York , USA) at the Austrian Centre for Electron Microscopy and Nanoanalysis. For investigating a rubicene crystal the AFM was operated in the intermittent-contact mode which allows to image the crystal's surface topography and also to record phase images of the surface.
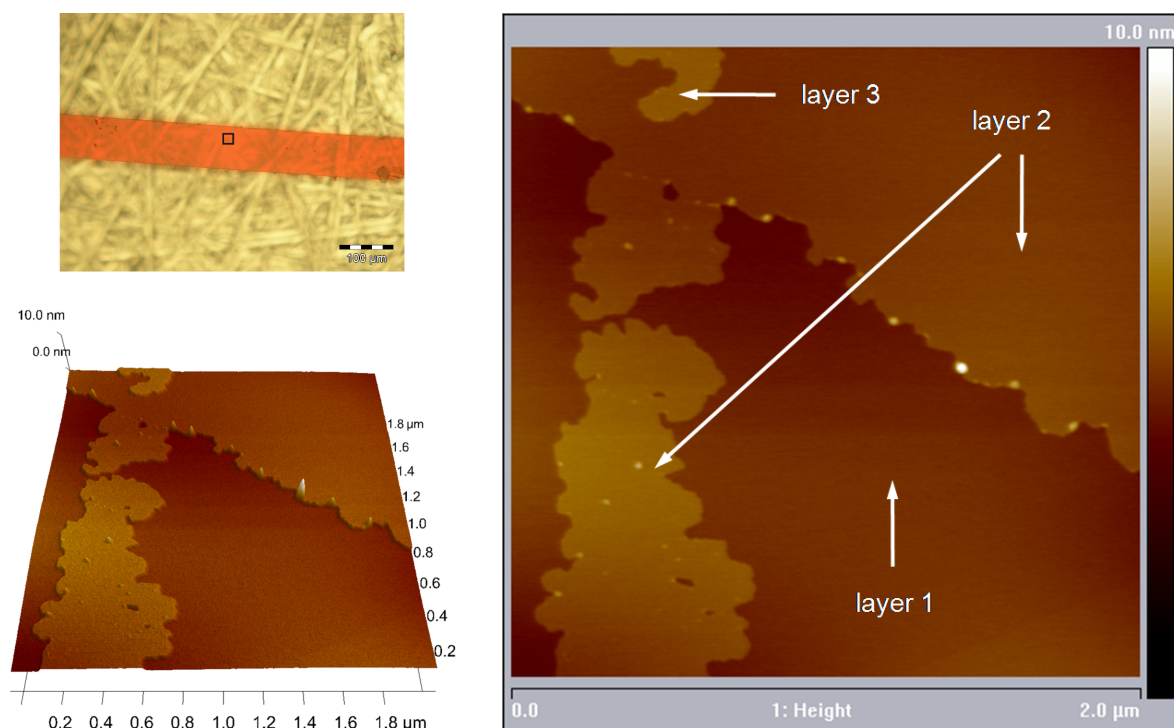
**Figure 3.10:** AFM height images acquired from the central area of a rubicene crystal's surface (marked in the image of the crystal on the top left). The lower left image gives a three-dimensional impression of the surface topography. On the right the layered terrace structure with three differently high layers is shown. The terrace height increases from layer 1 to layer 3.

### 3.2.2.1 Surface Topography

AFM height images of a rubicene crystal's surface topography are depicted in Figure 3.10 and Figure 3.11. Figure 3.10 shows a central area on the crystal surface where a layered terrace structure can be found. According to the colors in the height images there are differently high terraces grown on this surface area. The layered terraces appear to be extremely flat. In Figure 3.11 the surface topography of the crystal's border area near its edge is shown. Again a layered terrace structure is found. The terraces show the same characteristics as for the crystal's central area. Although the surface is ruptured in the vicinity of the rubicene crystal's edge the terrace growth continues around the crack. In all AFM height images a wavy overlay can be seen which is an artifact caused by laser reflections. The layered terrace structure unveiled with the AFM agrees well with the SEM results presented in Section 3.2.1.1. Due to the fact that the circular troughs on the crystal surface are only visible in SEM images (see Figure 3.4) but not in AFM height images one can assume that these troughs are attributable to the conductive coatings of the crystals for SEM imaging.
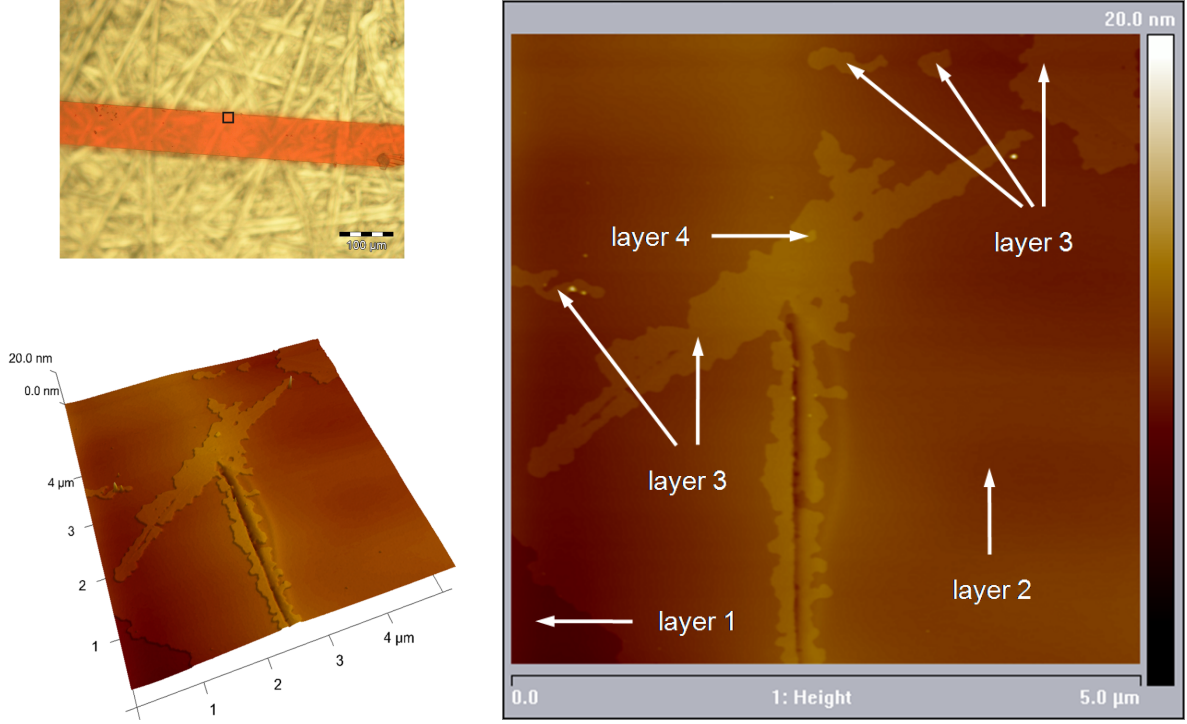
**Figure 3.11:** AFM height images acquired from the border area of a rubicene crystal's surface (marked in the image of the crystal on the top left). A three-dimensional representation of the border area's surface topography is depicted in the lower left image. One can notice a slight slope towards the edge of the crystal on the left side of the surface crack. The right image shows four layers of different heights, rising from layer 1 to layer 4. The layered terrace structure can be found even around the crack and across the slope.

The line section across a terrace step (see Figure 3.12) indicates terrace heights of approximately 1 nm. The same result is obtained from a height statistics plot of the same terrace step, which is depicted in Figure 3.13. It shows the height distribution of a surface area with this two differently high terraces. The height of the lower and the higher terrace is about 0.3 nm and 1.3 nm, respectively. The root mean squared roughness of the crystal surface can be calculated by use of the following equation:

$$R_{RMS} = \sqrt{\frac{1}{MN} \sum_{m=1}^{M} \sum_{n=1}^{N} [z(x_m, y_n) - \bar{z}]^2}, \tag{3.1}$$

with

$$\bar{z} = \frac{1}{MN} \sum_{m=1}^{M} \sum_{n=1}^{N} z(x_m, y_n), \tag{3.2}$$

the mean value of the height $z$ across all surface coordinates $(x, y)$. The calculation, which is
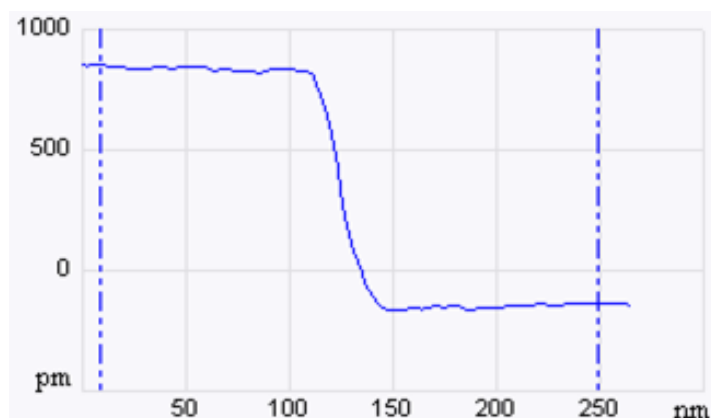
**Figure 3.12:** Line section across a terrace step on the rubicene crystal's surface. The ordinate's scale represents the absolute height values of the AFM's piezo scanner, with an arbitrary zero point. The graph is obtained after averaging over several adjacent line sections across the same terrace step.
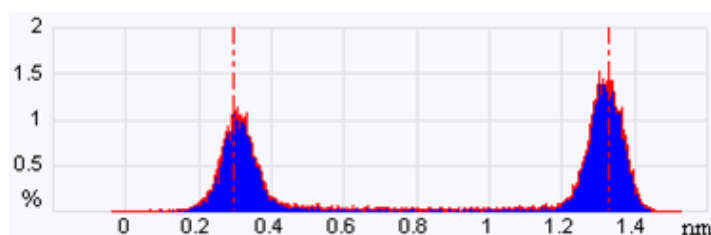


**Figure 3.13:** Height statistics of a surface area on the rubicene crystal. The data suggests two different terraces with a step height of approximately $1\,\mathrm{nm}$. The zero point of the height scale, which is assigned to the abscissa, corresponds to the highest point on the surface area investigated. Thus higher values mean lower surface areas. The broadening of the peaks is caused by noise due to the process of measuring.

done with the aid of the software used to do the AFM measurements, results in a root mean squared surface roughness between $0.4\,\text{Å}$ and $0.7\,\text{Å}$. These roughness values are very low and prove that the rubicene crystal's surface is extremely smooth.

### 3.2.2.2 Phase Images

The results from the PDM measurements are illustrated in Figure 3.14. The phase images of the rubicene crystal's surface are taken from the same central and the same border area as the AFM height images depicted in Figure 3.10 and Figure 3.11. The absence of any phase contrast in both phase images indicates practically the same mechanical properties for all surface layers. Inhomogeneities in the surface layers, such as crystallites or grains, would be visible in the phase images too, which isn't observed in our case.
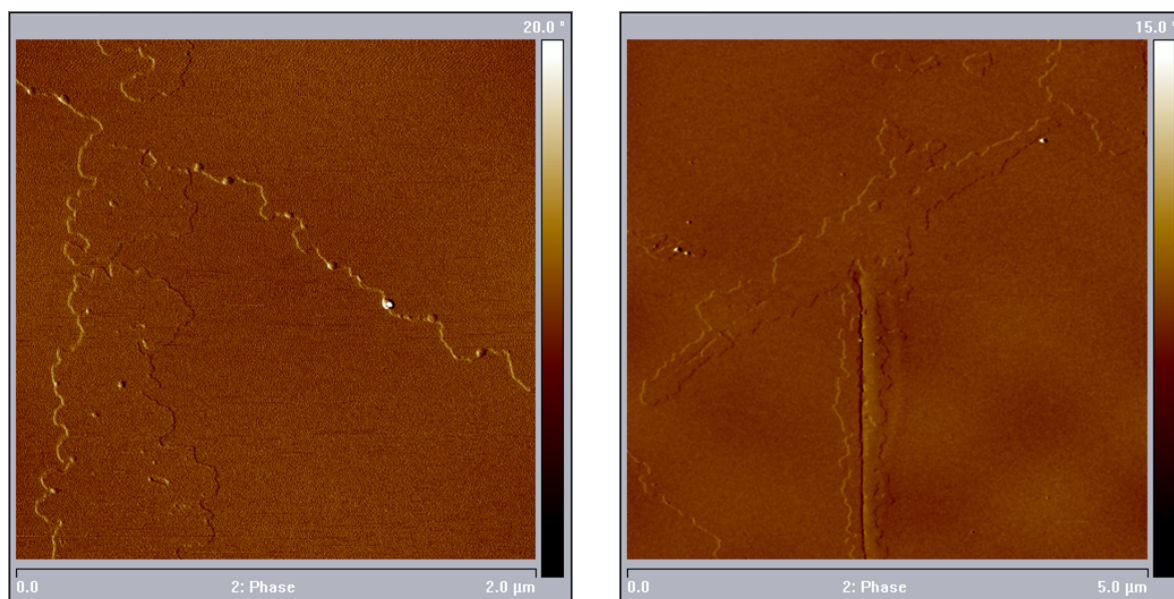
**Figure 3.14:** Phase images of the rubicene crystal's surface which are taken from the same two areas that are depicted in the AFM height images too. The central area is shown on the left side, the border area on the ride side.

### 3.2.3 Fourier Transform Infrared Spectroscopy

The fundamentals of FTIR spectroscopy are treated in [7, 11, 22]. IR spectroscopy is an analytical method which uses infrared light to investigate the specimen. Absorption features in the infrared region of the electromagnetic spectrum are characteristic for the molecular structure. Therefore IR spectroscopy provides crucial information on a specimen's compounds and atomic bonds. In case of organic materials the focus is mainly on bonds between carbon and hydrogen atoms.

The infrared part of the spectrum can be divided into three regions, the near-infrared (NIR, wavelength range: $0.8\,\mu m$ to $10\,\mu m$), the mid-infrared (MIR, wavelength range: $10\,\mu m$ to $40\,\mu m$) and the far-infrared (FIR, wavelength range: $40\,\mu m$ to $1000\,\mu m$). Whereas absorptions in the FIR-region are associated with rotations of molecules those in the wavelength range of MIR and NIR are due to vibrational excitations of atomic bonds or bonds of atom groups within the molecule. The absorptions occur at resonance frequencies of the corresponding bonds that vibrate and since these frequencies depend on the bond strengths and the masses of the atoms involved they are specific for the particular bond types. There are various possibilities for bonds to vibrate which are called vibrational modes, such as symmetric and antisymmetric stretching vibrations or different bending vibrations. Among all vibrational

modes only modes with a change in the molecular dipole moment can interact with the electromagnetic field of the incoming infrared light. Hence only these modes are detectable with IR spectroscopy. C-H stretching vibrations are very dominant in most organic molecules. Table 3.1 gives a review of some important C-H stretching vibrations and the respective spectral regions at which these vibrations absorb infrared light, according to [7, 11].

Although IR spectroscopy can be carried out in the same way as optical spectroscopy by use of dispersive elements like prisms and lattices, interferometrical methods have enforced since the development of FTIR spectroscopy. Thereby the light beam must no longer be split into its spectral components but instead the transmission of the entire beam through the specimen is measured. Basically a FTIR spectrometer consists of an IR source, a Michelson interferometer and an IR detector, as shown in Figure 3.15. Infrared light from the source is

**Table 3.1:** Characteristic absorptions of C-H stretching vibrations in the infrared spectral region.

| | C-H stretching vibrations | Spectral range of absorption / cm$^{-1}$ |
|---|---|---|
| Saturated hydrocarbons | $-\overset{\mid}{\underset{\mid}{C}}-H$ | 2880-2890 |
| | $\diagup\!\!\diagdown C \diagup\!\!\diagdown^{H}_{H}$  $\quad -\overset{H}{\underset{H}{C}}-H$ | 2850-2960 |
| Unsaturated hydrocarbons | $\diagup\!\!\diagdown C = C \diagup^{H}\diagdown$ | 3010-3040 |
| | $\diagup\!\!\diagdown C = C \diagup^{H}\diagdown_{H}$ | 3075-3095 |
| | $-C \equiv C - H$ | 3300 |

**Figure 3.15:** Schematic setup of a FTIR spectrometer.

collimated by a lens and then impinges on a beam splitter which generates two light beams of half the intensity of the incoming light beam. Thus there are two different light beams which get to the IR detector. One light beam reflects off the beam splitter towards a fixed mirror which is aligned perpendicular to the incident beam. There the beam is reflected back and then it partly passes through the beam splitter. Finally the beam is focused on the IR detector by a lens. The other light beam passes through the beam splitter and is reflected back by a movable mirror which again is aligned perpendicular to the incident beam. Once the beam returns to the beam splitter it is partly reflected off towards the final lens which focuses the beam on the IR detector. Usually the specimen is located before the final lens so that the infrared light passes through it. The incidence of the two light beams on the IR detector causes the appearance of two-beam interference and therefore the measured irradiance depends on the position of the movable mirror. If the source provides monochromatic light of certain intensity $I_{\tilde{\nu}}$, the superposition of two harmonic plane waves of same amplitude $\mathbf{E}_0$, angular frequency $\omega$ and propagation direction $\mathbf{k}$, but with a phase difference $\Delta\phi$,

$$\mathbf{E}_1 = \mathbf{E}_0 e^{i(\mathbf{k}\mathbf{r}-\omega t)} \qquad \text{and} \qquad \mathbf{E}_2 = \mathbf{E}_0 e^{i(\mathbf{k}\mathbf{r}-\omega t+\Delta\phi)}, \qquad (3.3)$$

results in the following irradiance $I$ on the detector:

$$I = \frac{I_{\tilde{\nu}}}{2}[1 + \cos(\Delta\phi)], \qquad \text{with } I_{\tilde{\nu}} = 4|\mathbf{E}_0|^2 \tag{3.4}$$

The phase difference $\Delta\phi$ depends on the wavenumber $\tilde{\nu}$ and the optical path difference $d$ between the two waves, according to:

$$\Delta\phi = 2\pi\tilde{\nu}d \tag{3.5}$$

Considering beams parallel to the optical axis and vacuum as medium (refractive index $n = 1$), the optical path difference $d$ is simply double the difference $x$ of the movable mirror's distance from the beam splitter compared to that of the fixed mirror. The irradiance $I$ on the detector varies as $x$ changes with the position of the movable mirror, yielding the following interferogram function:

$$I(x) = \frac{I_{\tilde{\nu}}}{2}[1 + \cos(4\pi\tilde{\nu}x)] \tag{3.6}$$

In the general case of polychromatic light with a spectral intensity distribution $I(\tilde{\nu})$ the interferogram function becomes:

$$I(x) = \frac{1}{2}\int_0^\infty I(\tilde{\nu})[1 + \cos(4\pi\tilde{\nu}x)]d\tilde{\nu} \tag{3.7}$$

The constant term in the equation above contains no spectral information and hence it can be omitted:

$$I'(x) = \frac{1}{2}\int_0^\infty I(\tilde{\nu})\cos(4\pi\tilde{\nu}x)d\tilde{\nu} \tag{3.8}$$

Finally a Fourier transform of this interferogram function leads to the intensity distribution of the recorded IR spectrum:

$$I(\tilde{\nu}) = \frac{1}{2\pi}\int_{-\infty}^\infty I'(x)\cos(4\pi\tilde{\nu}x)dx \tag{3.9}$$

Since in FTIR spectroscopy the light doesn't need to be separated into its spectral components nearly the whole intensity of the light beam gets to the IR detector, which significantly improves the signal-to-noise ratio. Additionally the whole spectrum is recorded at once and therefore the testing time is very short. It should be mentioned that the resolution of a FTIR spectrometer is limited by the maximum displacement $x_{max}$ of the movable mirror:

$$\Delta\tilde{\nu} = \frac{1}{2x_{max}} \tag{3.10}$$

The IR spectra were recorded in transmission mode and gathered with the aid of a Hyperion
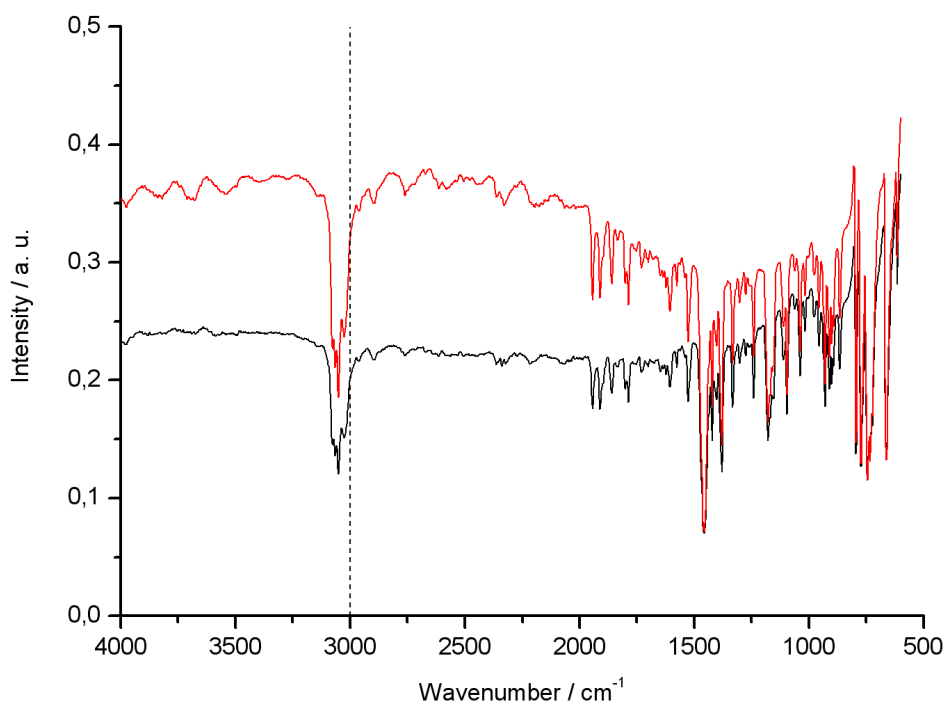
**Figure 3.16:** IR spectra of a rubicene crystal of high chemical purity, recorded at two different crystal positions (black and red curve). Both spectra show a distinct absorption peak above $3000\,\text{cm}^{-1}$. Additionally the red curve is superimposed by an interference pattern caused by the flat, parallel crystal surfaces.

3000 FTIR microscope equipped with an Equinox 55 spectrometer, both from Bruker Optics (Ettlingen, Germany), at the Austrian Centre for Electron Microscopy and Nanoanalysis.

### 3.2.3.1 Chemical Purity

IR spectra of a rubicene crystal are depicted in Figure 3.16. In each of these spectra, which correspond to two different crystal positions, the same absorption peak appears in a wavenumber range between $3000\,\text{cm}^{-1}$ and approximately $3100\,\text{cm}^{-1}$. Considering C-H stretching vibrations, absorption only occurs above $3000\,\text{cm}^{-1}$. As listed in Table 3.1 absorptions above $3000\,\text{cm}^{-1}$ belong to C-H stretching vibrations of unsaturated hydrocarbons. Rubicene is a polycyclic aromatic hydrocarbon and hence a rubicene molecule consists of a system of aromatic rings. Consequently only C-H stretching vibrations of unsaturated hydrocarbons should occur, which is exactly the situation represented in the IR spectra in Figure 3.16.
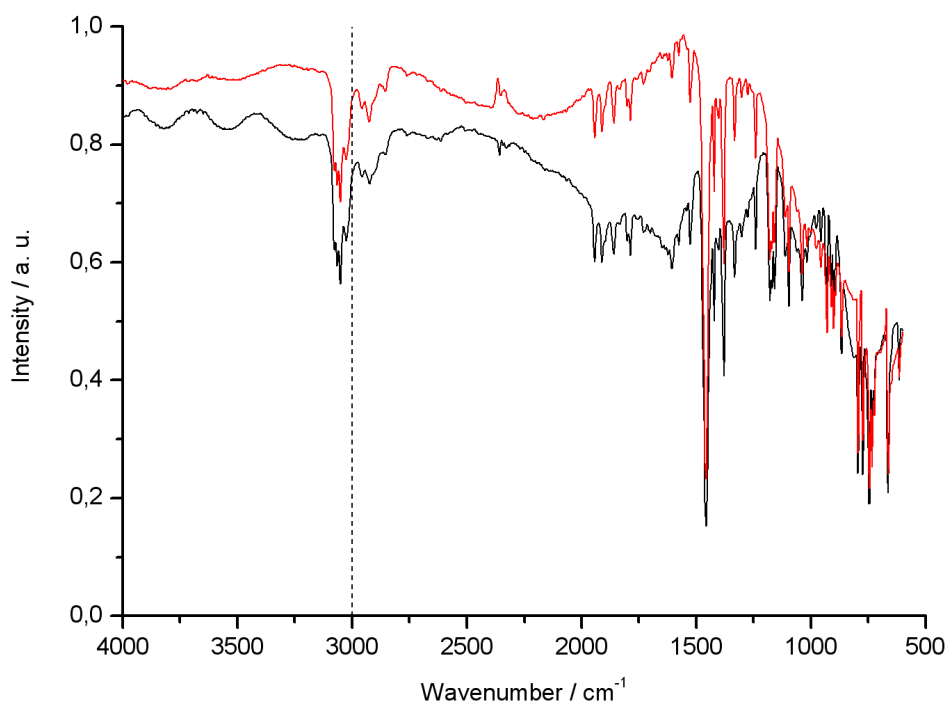
**Figure 3.17:** IR spectra of a chemically less pure rubicene crystal, recorded at two different crystal positions (black and red curve). Both spectra show the same absorption characteristics - a small peak below and a much more pronounced peak above $3000\,\mathrm{cm}^{-1}$. Furthermore the black curve is superimposed by an interference pattern caused by the flat, parallel crystal surfaces.

Therefore these spectra are a concrete evidence for the high chemical purity of this rubicene crystal.

Nevertheless not all of the grown rubicene crystals are chemically that pure. For instance the IR spectra depicted in Figure 3.17, again acquired from two different crystal positions, indicate a lower chemically purity of the rubicene crystal investigated. One can clearly identify two different absorption peaks around $3000\,\mathrm{cm}^{-1}$ in these spectra. Whereas the strongly pronounced peak above $3000\,\mathrm{cm}^{-1}$ corresponds to C-H stretching vibrations of unsaturated hydrocarbons, the less pronounced peak below $3000\,\mathrm{cm}^{-1}$ arises from the excitation of C-H stretching vibrations of saturated hydrocarbons, according to the data in Table 3.1. The occurrence of saturated hydrocarbons suggests the existence of either modified rubicene molecules or foreign molecules and therefore this rubicene crystal has a lower chemically purity.
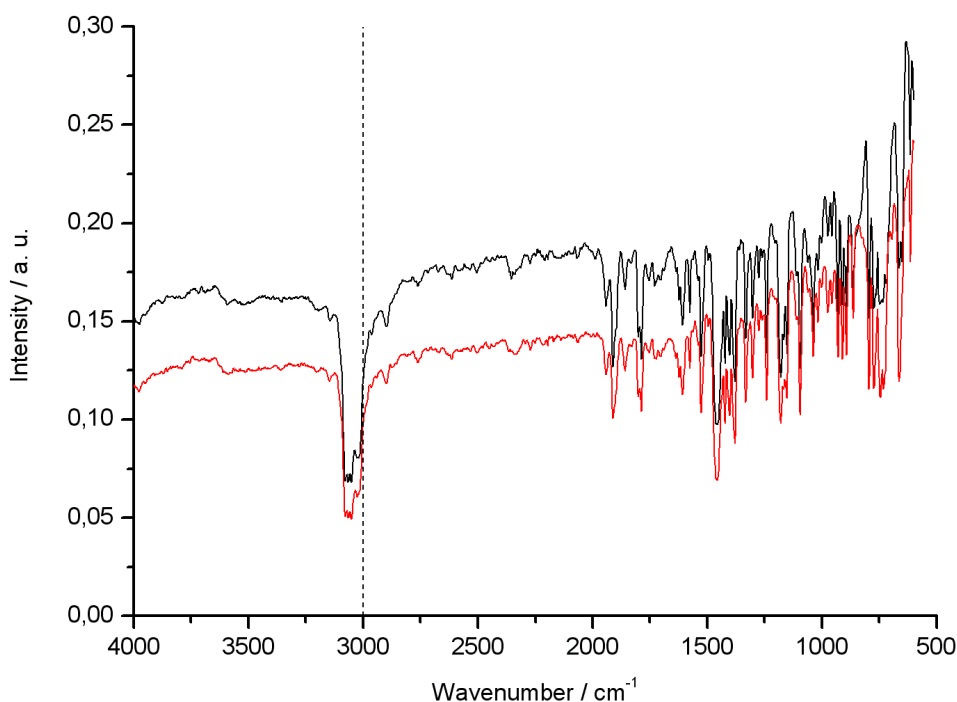
**Figure 3.18:** IR spectra of a rubicene crystal from Langhals, recorded at two different crystal positions (black and red curve). A distinct absorption peak above $3000\,\mathrm{cm^{-1}}$ is visible in both spectra.

For comparison Figure 3.18 shows IR spectra of a rubicene crystal from Langhals (Ludwig Maximilian University, Munich, Germany), which was grown from rubicene synthesized as described in [16]. The spectra correspond to two different positions of this crystal and indicate a high chemical purity due to the presence of absorption peaks only above $3000\,\mathrm{cm^{-1}}$.

## 3.3  Crystal Structure

For investigating the structure of the grown rubicene crystals the method of X-ray diffraction (XRD) is applied. Within materials science and solid state physics this is a well proven technique to determine the crystal structure of solids.

### 3.3.1 X-ray Diffractometry

The fundamentals of this section are deduced from [1, 21]. X-rays have a wavelength of the order of 0.01 nm to 1 nm, which also matches the atomic distances in solids. As a result the periodically arranged atoms of a crystal act like a three-dimensional diffraction grating for X-rays. Diffraction emerges as the incident X-rays are elastically scattered by parallel lattice planes in the crystal, in particular by the atomic electron shells. Subsequently the diffracted X-rays interfere with each other and, under certain conditions, constructive interference can occur.

Whether or not the diffracted X-rays interfere constructively is based on the so called Laue condition, which says that the scattering vector

$$\mathbf{\Delta k} = \mathbf{k}' - \mathbf{k}, \tag{3.11}$$

where $\mathbf{k}$ and $\mathbf{k}'$ are the wavevectors of the incident and the diffracted beam, respectively, has to be equal to a particular vector of the reciprocal lattice to obtain constructive interference:

$$\mathbf{\Delta k} = \mathbf{G}_{hkl} \tag{3.12}$$

Every vector of the reciprocal lattice is perpendicular to a lattice plane in real space. Thus the reciprocal lattice vector $\mathbf{G}_{hkl}$ is labeled with the Miller indices $(hkl)$ of the set of parallel lattice planes in real space which is perpendicular to it and from which, of course, the X-rays are diffracted. Because of the Laue condition the scattering vector has to be perpendicular to this set of lattice planes too and hence, in the case of elastic scattering, where $|\mathbf{k}| = |\mathbf{k}'|$, the angle $\theta$ between the incident beam and the lattice plane is equal to the angle between the diffracted beam and the lattice plane, as shown in Figure 3.19. Furthermore the absolute value of $\mathbf{G}_{hkl}$ is inversely proportional to the spacing $d_{hkl}$ between the parallel lattice planes:

$$|\mathbf{G}_{hkl}| = \frac{2\pi}{d_{hkl}} \tag{3.13}$$

Taking account of $|\mathbf{k}| = |\mathbf{k}'|$, Equation 3.12 can be transformed so that the Laue condition becomes:

$$2\mathbf{k}\mathbf{G}_{hkl} = -\mathbf{G}_{hkl}^2 \tag{3.14}$$

With Equation 3.13 and the absolute value of the wavevector,

$$|\mathbf{k}| = \frac{2\pi}{\lambda}, \tag{3.15}$$

which is proportional to the reciprocal of the wavelength $\lambda$, the Laue condition, as denoted
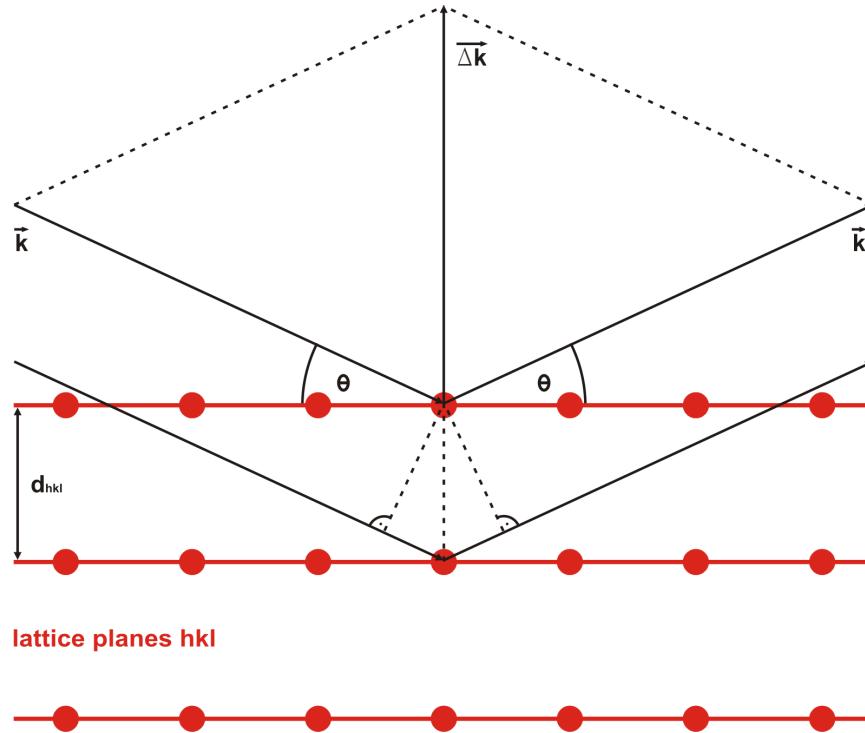
**Figure 3.19:** The incident X-ray beam, which propagates along **k**, is diffracted by a set of parallel lattice planes ($hkl$). The spacing between particular planes is $d_{hkl}$. After diffraction the X-ray beam propagates along **k′**.

in Equation 3.14, can be rewritten and one obtains the following, non vectorial form:

$$\lambda = 2d_{hkl}\sin(\theta) \tag{3.16}$$

This is the so called Bragg's law. Supplementary Bragg's law can be deduced from a completely geometrical approach. As visible in Figure 3.19 the lower diffracted beam has an overall longer path. The optical path difference between the upper and the lower diffracted beam, which can be calculated easily with geometrical considerations, has to be an integer multiple of the wavelength $\lambda$ to get constructive interference:

$$n\lambda = 2d_{hkl}\sin(\theta) \tag{3.17}$$

Except for the integer $n$ Equations 3.16 and 3.17 are identical. In summary, it can be stated that the Laue condition determines the two essential requirements for constructive interference of the diffracted X-rays. On the one hand the scattering vector has to be perpendicular to the diffractive lattice planes and on the other hand Bragg's law has to be fulfilled. Only if both requirements are satisfied there will be constructive interference which results in detectable intensity of the diffracted X-rays.

Practically a X-ray diffractometer is used to determine the specimen's crystal structure by measuring the intensities of the diffracted X-rays. Basically it consists of a source to generate the X-rays, typically a X-ray tube, a goniometer on which the specimen is mounted and a detector to collect the diffracted intensities, usually a CCD-detector. Furthermore the X-rays from the source pass through a monochromator and a collimator to form a primary beam with the characteristic wavelength of the X-ray source. Once the primary beam hits the specimen it is diffracted into various directions. Whether constructive interference occurs in any direction only depends on the relative position between the primary beam and the lattice planes involved and on the spacing between these lattice planes, according to Bragg's law. Since constructive interference of the diffracted X-rays is possible in any direction the specimen has to be rotated. This is done with special 3- or 4-circle goniometers, which allow to rotate the specimen in space. Additionally the detector can be turned too. For measuring the diffracted intensities a certain angle $2\theta$ is set between the primary beam and the detector. In this way Bragg's law is always fulfilled for a set of parallel lattice planes with a specific spacing $d_{hkl}$. Subsequently the specimen is rotated in all directions so that every set of parallel lattice planes is once perpendicular to the scattering vector $\Delta \mathbf{k}$ and, if the planes' spacing matches the selected spacing $d_{hkl}$, the diffracted X-rays interfere constructively, resulting in intensity on the detector. Then a set of parallel lattice planes with another spacing $d_{hkl}$ is chosen by changing the angle $2\theta$, according to Bragg's law, and again the specimen is rotated in all directions to probe all lattice planes.

The XRD measurements were carried out on a Kappa Apex II X-ray diffractometer from Bruker AXS (Karlsruhe, Germany) at the Institute for Chemistry and Technology of Materials. This instrument uses a X-ray tube with a molybdenum anode which generates X-rays with a characteristic wavelength of 0.71 Å. Moreover it can envelope the specimen in a cold nitrogen gas stream to permit crystallographic studies at low temperatures which improve the accuracy of the structural data.

In the course of XRD four grown rubicene crystals as well as a rubicene crystal from Langhals, which was grown from rubicene synthesized as described in [16], were investigated. All crystals were measured at a temperature of 100 K. Additionally one grown rubicene crystal was measured at a temperature of 250 K.

### 3.3.1.1 Crystal System

XRD reveals that the crystal structure of a rubicene crystal is monoclinic and its Bravais lattice is primitive monoclinic. Figure 3.20 depicts the packing of the molecules in a rubicene
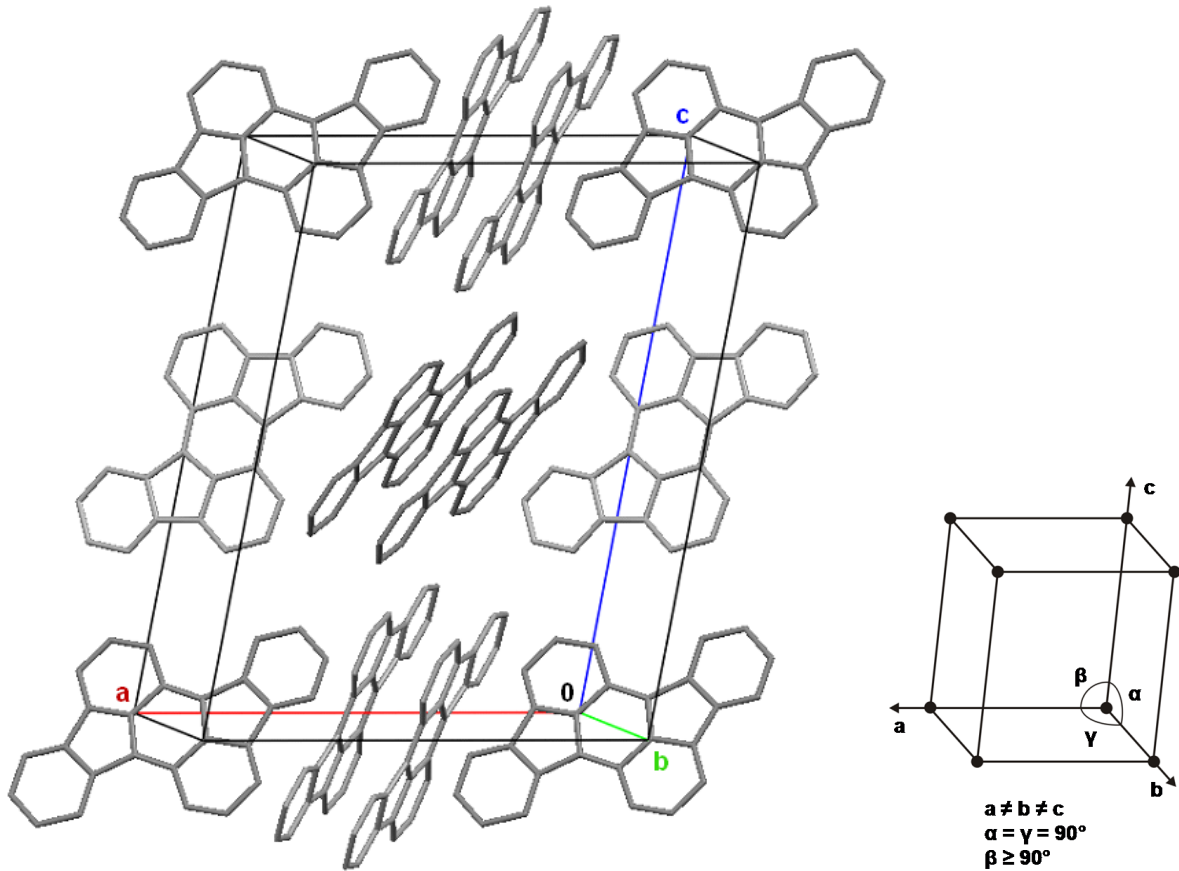
**Figure 3.20:** Packing of the molecules in a rubicene crystal together with the crystal's unit cell. On the right the properties of the primitive monoclinic Bravais lattice are displayed.

crystal. In addition the unit cell of the crystal's lattice is shown. According to a primitive monoclinic lattice all three lattice vectors of the unit cell are unequally long and two of the three angles between the lattice vectors are equal to 90°. From the unit cell's dimensions its volume can be calculated, according to:

$$V = abc \sin(\beta) \tag{3.18}$$

In the case of a rubicene crystal four rubicene molecules form the basis, which is attached to each lattice point of the primitive monoclinic lattice. Since the unit cell of a primitive monoclinic lattice consists of just one lattice point, the unit cell of a rubicene crystal contains four formula units, namely four rubicene molecules, as shown in Figure 3.21. With knowledge of the number $Z$ of formula units per unit cell, the unit cell's volume $V$ and the molar mass $M$ of a rubicene molecule the density of a rubicene crystal can be obtained from the following
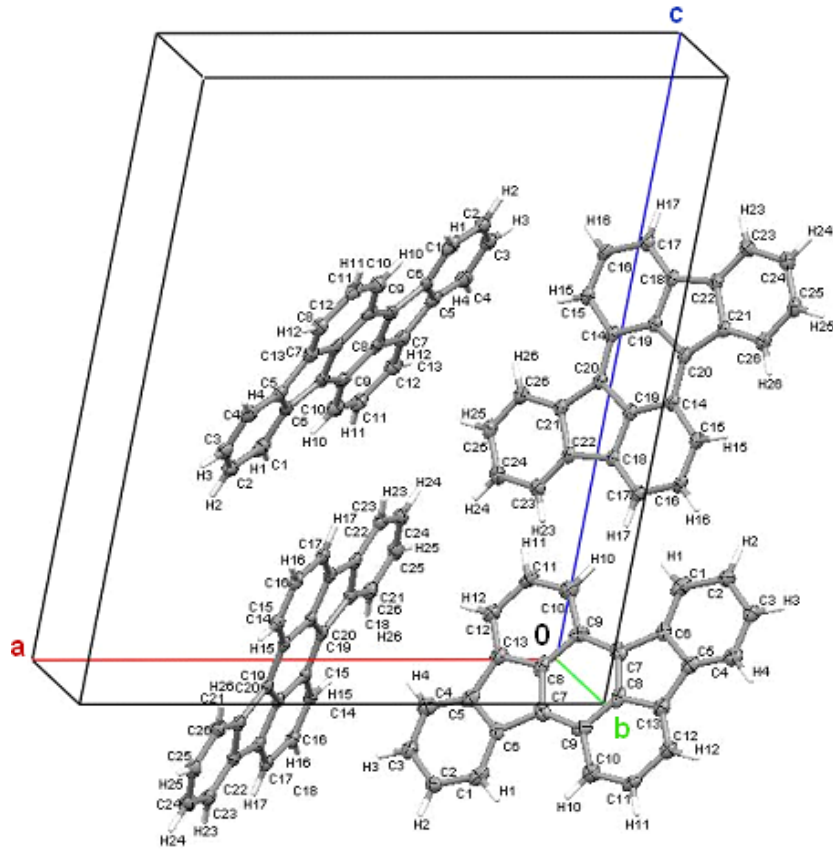
**Figure 3.21:** Unit cell of a rubicene crystal with four rubicene molecules, which form the basis.

equation, where $N_A$ is the Avogadro constant:

$$\rho = \frac{ZM}{N_A V}, \qquad \text{with } N_A = 6.022 \cdot 10^{23} \, \text{mol}^{-1} \tag{3.19}$$

Based on the experimentally determined XRD data the dimensions of the unit cell can be calculated. For refinement of the measured values a least-squares fit is performed. The reliability factor $R$ is used to define how far the fitted data agree with the observed data:

$$R = \frac{\sum_{hkl} ||F_o| - |F_c||}{\sum_{hkl} |F_o|}, \tag{3.20}$$

where $F_o$ and $F_c$ are the observed and the calculated structure factors, respectively. The sums extend over all measured data points. Consequently proper XRD measurement results are characterized by small reliability factors.

**Table 3.2:** XRD results of the rubicene crystals investigated.

| | |
|---|---|
| $T$ | Temperature ($\Delta T = 2\,\text{K}$) |
| $\theta$-range | $\theta$-range for data collection |
| $R$ | Reliability factor for all data (according to Equation 3.20) |
| $a, b, c$ | Lattice parameters |
| $\alpha, \beta, \gamma$ | Angles between lattice basis vectors |
| $V$ | Volume of the unit cell (according to Equation 3.18) |
| $\rho$ | Density of the rubicene crystal (according to Equation 3.19) |

| | $T$ / K | $\theta$-range / $^\circ$ | $R$ | $a$ / Å | $b$ / Å | $c$ / Å |
|---|---|---|---|---|---|---|
| Crystal 1 | 100 | 1.57 - 24.99 | 0.0806 | 15.98 | 5.11 | 19.06 |
| | 250 | 1.56 - 25.00 | 0.0928 | 16.16 | 5.12 | 19.11 |
| Crystal 2 | 100 | 1.57 - 24.99 | 0.0742 | 15.98 | 5.11 | 19.06 |
| Crystal 3 | 100 | 1.77 - 20.00 | 0.1169 | 16.07 | 5.13 | 19.08 |
| Crystal 4 | 100 | 1.56 - 20.00 | 0.0945 | 15.99 | 5.13 | 19.19 |
| Crystal 5 (Langhals) | 100 | 2.15 - 20.00 | 0.1129 | 15.94 | 5.12 | 19.13 |

| | $T$ / K | $\alpha$ / $^\circ$ | $\beta$ / $^\circ$ | $\gamma$ / $^\circ$ | $V$ / Å$^3$ | $\rho$ / g/cm$^3$ |
|---|---|---|---|---|---|---|
| Crystal 1 | 100 | 90 | 97.26 | 90 | 1544.7 | 1.403 |
| | 250 | 90 | 97.22 | 90 | 1569.5 | 1.381 |
| Crystal 2 | 100 | 90 | 97.26 | 90 | 1544.7 | 1.403 |
| Crystal 3 | 100 | 90 | 97.46 | 90 | 1559.7 | 1.390 |
| Crystal 4 | 100 | 90 | 97.42 | 90 | 1560.6 | 1.389 |
| Crystal 5 (Langhals) | 100 | 90 | 97.46 | 90 | 1546.2 | 1.402 |

Table 3.2 list the results of the XRD measurements for all five rubicene crystals. It's obvious that the structure of all crystals is the same. Moreover the structural results of crystal 1, which was measured at a temperature of $100\,\text{K}$ as well as at a temperature of $250\,\text{K}$, are almost the same. This means that neither a phase transition nor a significant change in the crystal structure occur in a temperature range between $100\,\text{K}$ and $250\,\text{K}$. Additionally the smaller reliability factor of the data at $100\,\text{K}$ confirms that more accurate results are obtained at low temperatures. Considering all crystals the structural results of crystal 2 are the most accurate since they exhibit the smallest reliability factor. For that reason the remarks in Sections 3.3.1.2 and 3.3.1.3 are based on the XRD results of rubicene crystal 2.

### 3.3.1.2 Intramolecular Distances

Considering the intramolecular distances there are two different rubicene molecules among the four molecules of the basis. Figure 3.22 shows rubicene molecule 1 and its positions within the basis. The length of this rubicene molecule is 11.074 Å. In Figure 3.23 rubicene molecule
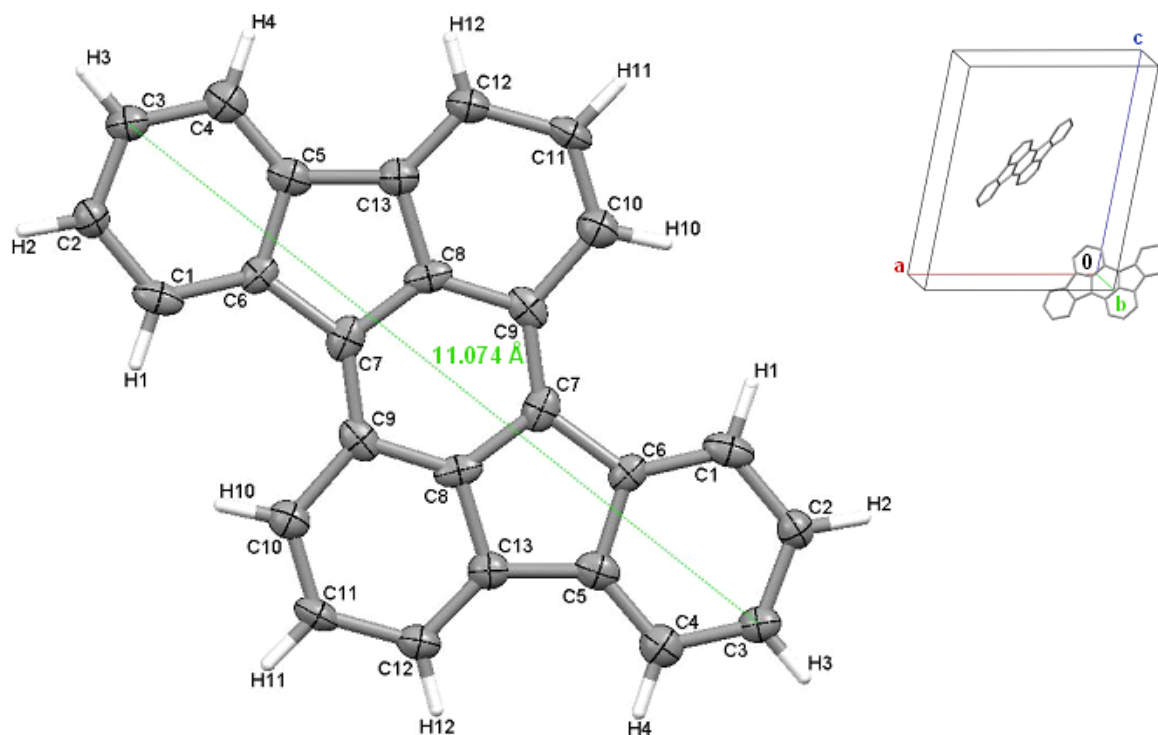
**Figure 3.22:** Structure and basis positions of rubicene molecule 1. The molecule's length is measured between the two carbon atoms which are furthest from each other.

2 and its basis positions are depicted. It has a length of 11.134 Å and thus it is slightly longer than rubicene molecule 1. The intramolecular distances of rubicene molecule 1 and rubicene molecule 2 can be seen in Figures 3.24 and 3.25, respectively.

### 3.3.1.3 Intermolecular Distance

The interplanar distance between two adjacent parallel molecules in the rubicene crystal is 3.347 Å, as illustrated in Figure 3.26. This intermolecular distance is small compared to other organic crystals and suggests a high atomic packing factor. For instance Jurchescu et al. [8] mention an interplanar distance of 3.654 Å between two adjacent parallel molecules, along the $\pi$-stack, in a rubrene single crystal at a temperature of 100 K. Finally, for comparison, the interplanar distance between the layers in graphite is 3.35 Å, as noted by Cotton et al. [4].

**Figure 3.23:** Structure and positions within the basis of rubicene molecule 2. The length of the molecule is measured between the two carbon atoms which are furthest from each other.



**Figure 3.24:** Intramolecular distances of rubicene molecule 1. Equivalent atoms are generated by symmetry transformations and hence their distances are identical.

**Figure 3.25:** Intramolecular distances of rubicene molecule 2. Equivalent atoms are generated by symmetry transformations and hence their distances are identical.



**Figure 3.26:** Intermolecular distance between two adjacent parallel rubicene molecules of a rubicene crystal.

## 3.4 Spectroscopy of Molecules in Solution

In general spectroscopic measurements of molecules in a solution deal with the interaction between these molecules and electromagnetic radiation of known wavelength, respectively of known energy. The molecules' response to the radiation is recorded as spectrum. It must be considered that the solvent's molecules also interact with the radiation and haven an influence on the spectrum. If visible or ultraviolet light is used for spectroscopy the quantized energy levels of molecules can be analyzed through transmittance spectra as well as excitation and emission spectra.

### 3.4.1 Solution Preparation

For spectroscopic investigations of rubicene molecules in solutions twice refined rubicene powder is used. It is obtained starting from rubicene powder with a purity of 98 % (the same as for the growth of rubicene crystals) via gas transport sublimation. Then the refined powder is dissolved in toluene (purity: $\geq 99 \%$) by use of a magnetic stirrer (Monotherm from Variomag, Daytona Beach, USA). Previously the amount of rubicene powder for the rubicene-toluene solution is defined precisely with the aid of an electric precision balance (ALC from Acculab Sartorius AG, Göttingen, Germany). The amount of toluene in the solution is controlled through a scaled syringe. In doing so rubicene-toluene solutions with a specific concentration (e.g. a concentration of 0.01 mg/ml is used for the spectroscopic measurements) can be realized. In addition the toluene is filtered through a 0.22 μm syringe filter in order to prevent from unwanted aggregates and impurities in the solution. Finally the rubicene-toluene solution is poured into a quartz cuvette to make spectroscopic measurements possible. Before that the cuvette is thoroughly cleaned with isopropyl alcohol and dried by a $CO_2$ gas flow. The light path through all quartz cuvettes used within the scope of this thesis is 10 mm.

### 3.4.2 Transmittance

If light traverses a medium it is attenuated due to absorption and scattering processes within the medium as well as reflections at the interfaces. The amount of the light's initial intensity $I_0$ which remains after passing through a medium with an attenuation coefficient $\mu$, where $x$ is the light's path length in the medium, is governed by Lambert's law:

$$I = I_0 e^{-\mu x} \tag{3.21}$$

The absorbance $A$ is defined as follows:

$$A = -\lg(\frac{I}{I_0}), \qquad \text{thus } A \propto \mu \tag{3.22}$$

Furthermore the transmittance $T$ represents that fraction of incident light that passed through the medium:

$$T = \frac{I}{I_0} \tag{3.23}$$

It's possible to determine this quantity experimentally and thereof the absorbance of the medium can be calculated from Equation 3.22. Moreover if scattering effects and reflections are negligible the attenuation coefficient $\mu$ in Equation 3.21 can be replaced by the absorption coefficient $\alpha$. In this case the absorbance represents the light's absorption within the medium.

The transmittance measurements were carried out on a Lambda 9, a dual beam spectrometer manufactured by Perkin-Elmer (Waltham, USA). This spectrometer features two monochromators, each provided with two gratings, one with 1440 lines/mm for the ultraviolet and the visible spectral range and one with 360 lines/mm for the NIR range of the spectrum. It uses a deuterium lamp for the ultraviolet and a halogen lamp for the visible and the NIR spectral region. A photomultiplier detects ultraviolet and visible light whereas a lead sulfide detector is used for NIR light. For the transmittance measurements within the scope of this thesis only the halogen lamp and the photomultiplier are used. It's crucial that the concentration of the rubicene-toluene solution investigated isn't too high. Otherwise saturation of absorption can lead to incorrect spectra. In this case the solution has to be diluted further. Before recording a transmittance spectrum a background correction of the spectrometer is performed without a specimen.

Figure 3.27 depicts the transmittance spectrum of a rubicene-toluene solution with a concentration of 0.01 mg/ml. According to Equation 3.22 this transmittance spectrum yields the absorbance spectrum shown in Figure 3.28. Since the toluene is filtered only scattering centers, e.g. aggregates or fine particles, with diameters below 0.22 µm exist in the solution. Considering the wavelength range of interest these scattering centers have no influence on the measurements. The spectrometer's geometry allows the incident light beam to impinge perpendicular on the quartz cuvette containing the rubicene-toluene solution. Reflections at the interfaces also attenuate the light as it passes through the cuvette. However this contribution to the light's overall attenuation is constant in the wavelength range considered and therefore it isn't crucial for investigations of the molecules' electronic structure. Thus the absorbance spectrum represents nothing more than the absorption properties of the solution. The sharp rise at approximately 550 nm denotes the absorption edge of the rubicene-toluene solution.
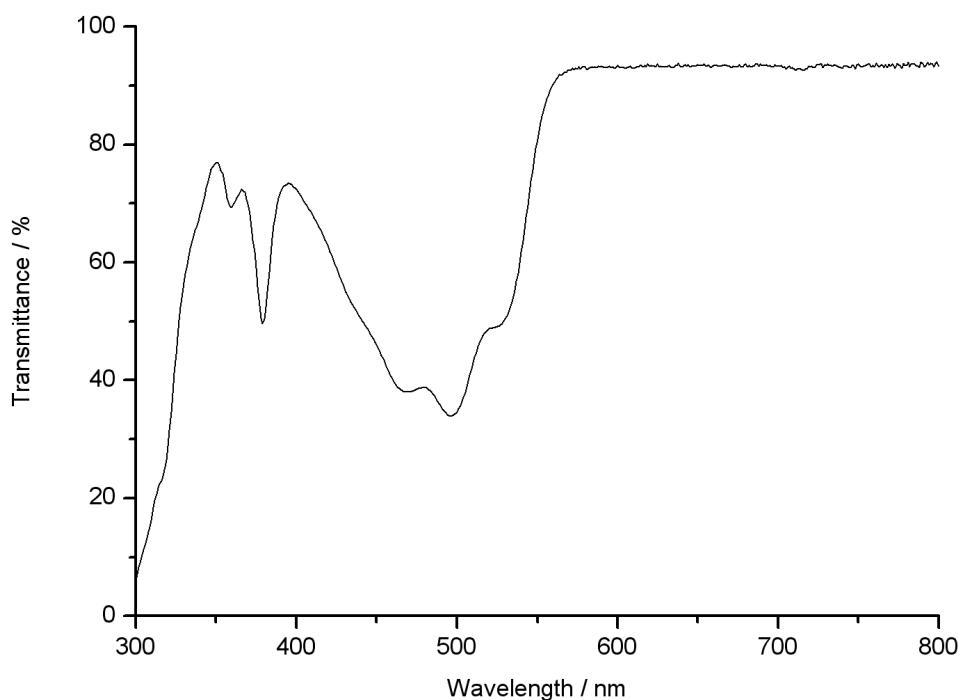
**Figure 3.27:** Transmittance spectrum of a rubicene-toluene solution (concentration: 0.01 mg/ml).

### 3.4.3 Photoluminescence

Luminescence is the spontaneous emission of electromagnetic radiation which takes place if electrons in atoms or molecules return from an excited state to the ground state and recombine with empty level positions or holes. The excitation of electrons into energetically higher states requires additional energy which can be absorbed in many ways. Depending on the kind of excitation energy a distinction is made between different types of luminescence. In the case of photoluminescence the excitation happens due to the absorption of photons. Therefore photoluminescence can be regarded as the opposite process of light absorption. Whereas a photon excites an electron into a energetically higher state in the process of light absorption, thereby being dissipated, a photon is generated as an excited electron returns to the ground state in the process of photoluminescence. In general luminescence can be divided into fluorescence and phosphorescence. Fluorescence is the spontaneous emission of light as an electron returns from an excited state to the ground state without a change in the spin multiplicity. Usually fluorescence transitions occur very fast, within nanoseconds or even picoseconds. Contrary phosphorescence is the light emission during a transition from
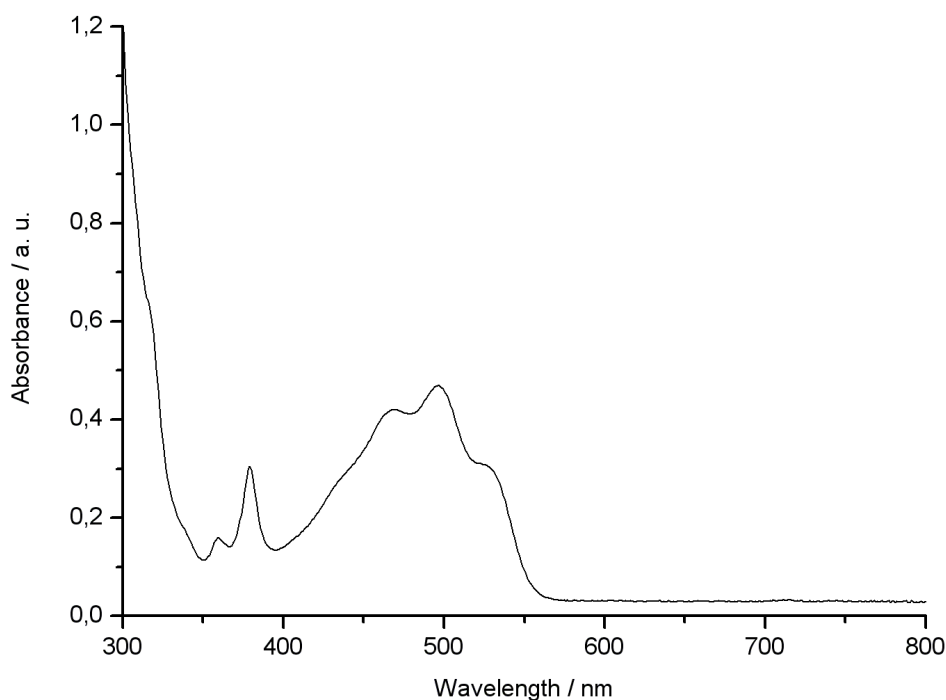
**Figure 3.28:** Absorbance spectrum of a rubicene-toluene solution (concentration: 0.01 mg/ml).

an excited state to the ground state involving a change in the spin multiplicity. Due to the spin flip phosphorescence transitions aren't as fast as fluorescence transitions. They occur after microseconds or later. Some materials even exhibit phosphorescence durations of several hours.

The photoluminescence excitation and emission spectra were obtained using a RF-5301PC spectrofluorophotometer from Shimadzu (Kyoto, Japan) which applies two monochromators, one for the excitation light and one for the emission light. Both monochromators operate with gratings with 1300 lines/mm. The spectrofluorophotometer uses a xenon lamp for illumination and a photomultiplier as detector. The instruments's setup allows the emission to be measured perpendicular to the excitation beam. Due to the fact that stray light leads to incorrect spectra the specimen has to be placed in such a way that the excitation beam isn't reflected directly from the specimen into the entrance slit of the detection unit. For photoluminescence emission measurements the wavelength of the excitation light is fixed at the absorption maximum to get maximum emission intensity. Similarly photoluminescence excitation spectra are recorded at a fixed emission wavelength. In the case of optically dense
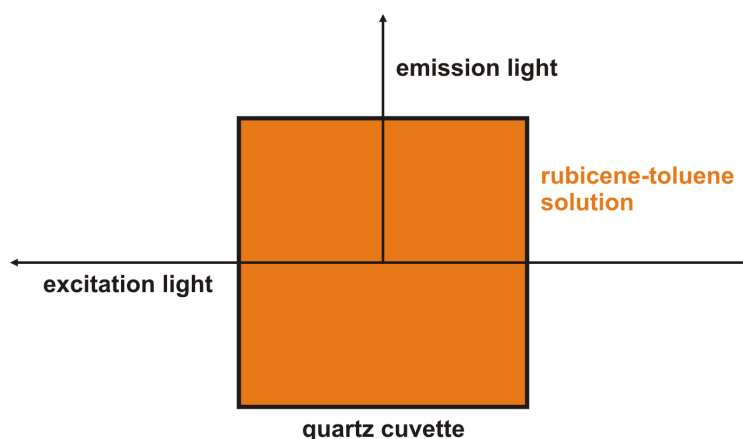
**Figure 3.29:** Top view on the 90° measurement setup in the spectrofluorophotometer, drawn schematically.

solutions self-absorption of the fluorescence light within the solution might cause an attenuation of the photoluminescence emission spectrum at the spectrum's short wavelength end where emission and absorption spectrum overlap. The photoluminescence excitation spectrum is also affected by optically dense solutions. A strongly absorbed wavelength of the excitation light is expected to yield a high emission intensity. However in an optically dense solution the intensity of the excitation light at such a strongly absorbed wavelength can get very low after a short distance through the solution. Thus the excitation intensity at the recorded area of the solution might be already too low to generate a high emission intensity, although the excitation wavelength is strongly absorbed. Since both types of photoluminescence spectra are susceptible to optically dense solutions a rather low concentration of the rubicene-toluene solution has to be preferred. Figure 3.29 schematically depicts the measurement setup for a rubicene-toluene solution in the spectrofluorophotometer.

Figure 3.30 depicts the photoluminescence excitation and emission spectra of the rubicene-toluene solution. Supplementary the solution's excitation spectrum is compared to its absorbance spectrum in Figure 3.31, both plotted versus the energy to determine the energy gap of a rubicene molecule. It's obvious that the structure of both spectra is the same. Moreover the almost identical absorption edges of these spectra indicate an energy gap of about 2.25 eV between the highest occupied molecular orbital (HOMO) and the lowest unoccupied molecular orbital (LUMO) of a rubicene molecule.
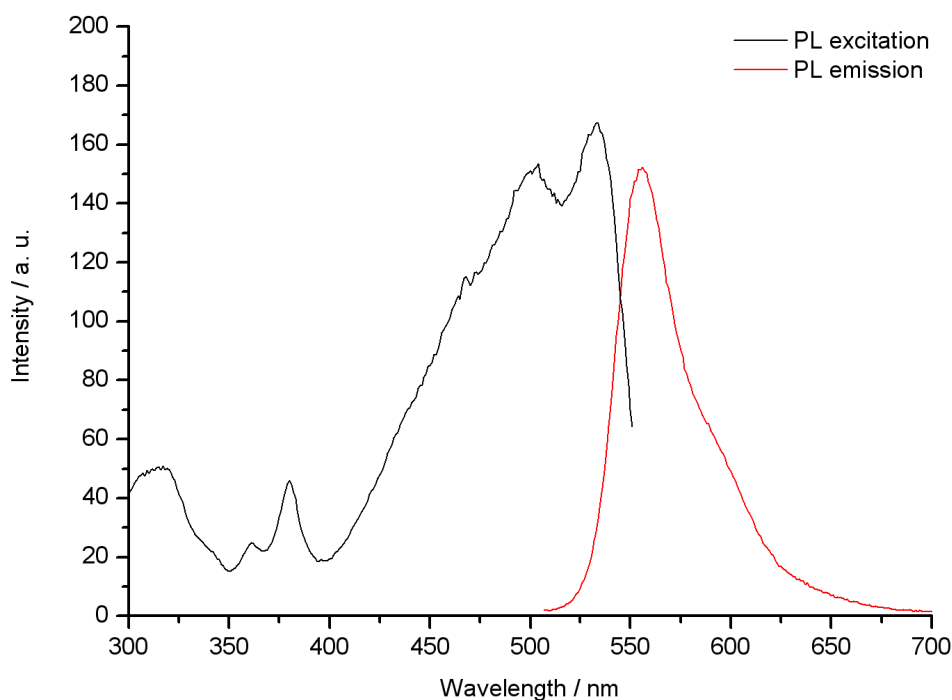
**Figure 3.30:** Photoluminescence (PL) excitation and emission spectra of a rubicene-toluene solution (concentration: 0.01 mg/ml). The emission wavelength for the excitation spectrum is set to 556 nm. The excitation wavelength for the emission spectrum is 502 nm.

## 3.5 Spectroscopy of Molecules in Solid State

In contrast to molecules in a solution there are stronger interactions between the molecules arranged in a crystal due to intermolecular forces which bind the crystal. These interactions lead to a broadening of the energy levels in the crystal, especially in case of higher levels which are far more affected by the influence of neighboring atoms than lower ones. Spectroscopic investigations in the visible and ultraviolet spectral range can provide insight into the specific electronic structure of a crystal.
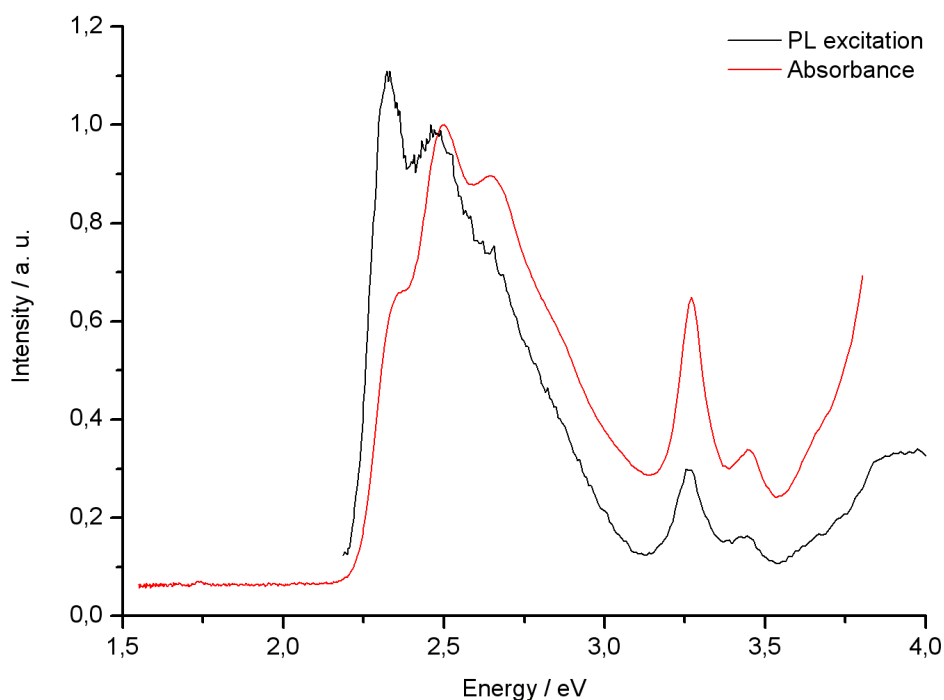
**Figure 3.31:** Comparison of the photoluminescence (PL) excitation spectrum and the absorbance spectrum of a rubicene-toluene solution (concentration: 0.01 mg/ml). The emission wavelength for the excitation spectrum is 600 nm. Both spectra are normalized with respect to the peak at 2.5 eV.

### 3.5.1 Transmittance

The basics of transmittance measurements are explained in Section 3.4.2. In contrast to solutions in cuvettes the transmittance of a rubicene crystal can't be measured with the Lambda 9 spectrometer because of the crystal's small dimensions. Therefore alternative measurement setups are necessary. A simple start-up method to determine the transmittance of a rubicene crystal was performed by use of a S2000, a miniature fiber optic spectrometer from Ocean Optics (Dunedin, Florida) which features a grating with 600 lines/mm and a CCD-array as detector. For recording a transmittance spectrum the crystal is attached to the spectrometer's optical fiber, across the circular entrance window, via vaseline (see Figure 3.32). Another optical fiber is mounted in such a way that its entrance window is face to face to that of the optical fiber with the rubicene crystal, approximately a centimeter apart. The second optical fiber is used to illuminate the crystal with light from a halogen lamp. First the spectrum of the light which traversed through the rubicene crystal is measured. Then the crystal is
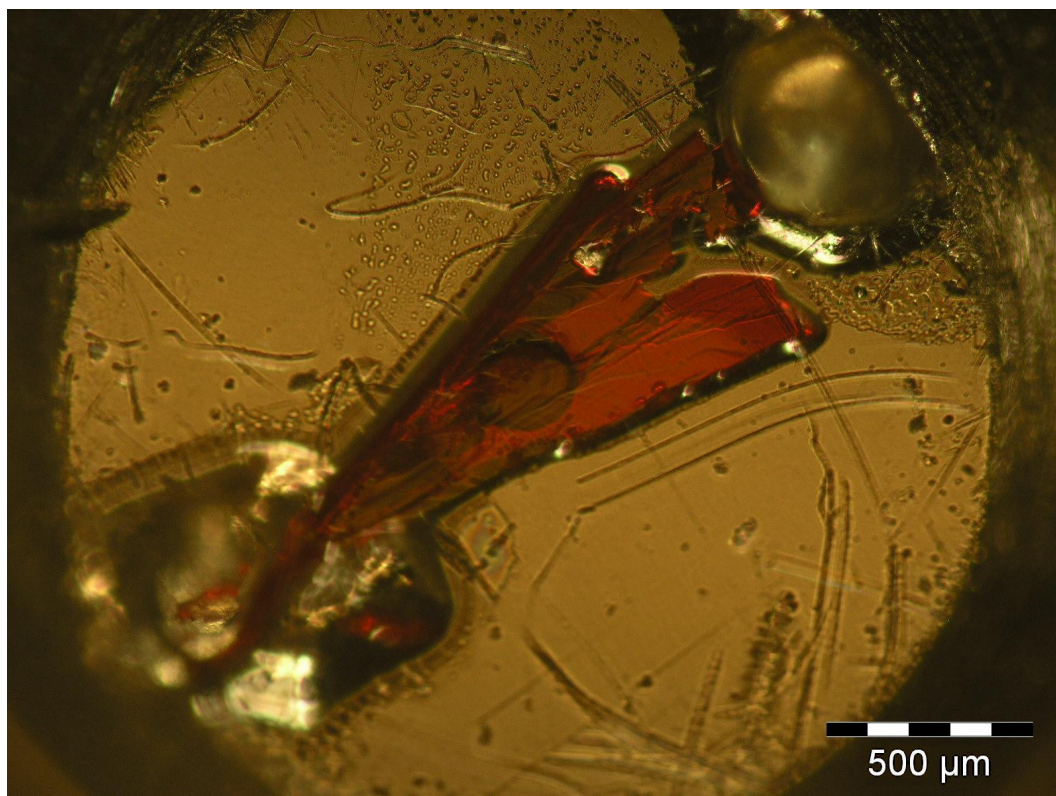
**Figure 3.32:** Rubicene crystal attached to the optical fiber of the spectrometer. The crystal completely covers the circular entrance window in the middle of the optical fiber. Vaseline, the gel-like substance at the ends of the crystal, is used for fixation.

removed and a reference spectrum of the halogen lamp is recorded. Thereby the setup must not change. From these two spectra the transmittance spectrum can be calculated, according to Equation 3.23.

In a more sophisticated setup the transmittance of a rubicene crystal was measured by use of a microscope, namely an IR-Plan infrared microscope from Spectra-Tech (Shelton, USA). For operating with the microscope it's necessary to put the crystal on a glass substrate. In fact the rubicene crystal is placed across a drilled hole on the glass substrate (see Figure 3.33) to avoid interference occurring from the parallel glass surfaces or from a possible air gap between the crystal and the glass substrate as the rubicene crystal is illuminated from bottom up in the microscope with light provided from a halogen lamp. Employing two apertures, one for the condenser and one for the objective, a specific area on the crystal surface can be selected. The light which passes through the selected area of the crystal is finally directed to an optical fiber via the microscope's optics. The optical fiber is linked to a MS125 spectrometer from Oriel Instruments (Stratford, USA) with a grating with 600 lines/mm. An advantage of

this spectrometer is its CCD-detector which can be cooled to minimize the noise caused by the detector and thus improve the signal-to-noise ratio. Within the scope of this thesis the cooler of the CCD-detector is set to $-20\,^{\circ}\mathrm{C}$ during all measurements with this spectrometer. The rubicene crystal's transmittance spectrum is acquired similarly to the method with the crystal attached to an optical fiber, which is mentioned above. First a spectrum with the rubicene crystal in the light path of the microscope is recorded. Afterwards a reference spectrum without crystal is taken. In accordance with Equation 3.23 both spectra yield the transmittance spectrum.

Figure 3.34 shows the transmittance spectra of two different rubicene crystals obtained with the aid of the measurement setups described above. It's obvious that both spectra illustrate the same result. The corresponding absorbance spectra, derived from these transmittance spectra according to Equation 3.22, are depicted in Figure 3.35. During the measurements reflections from the crystal can be neglected because the incident light beam impinges perpendicular on the crystal surface for both setups. Assuming further that scattering effects
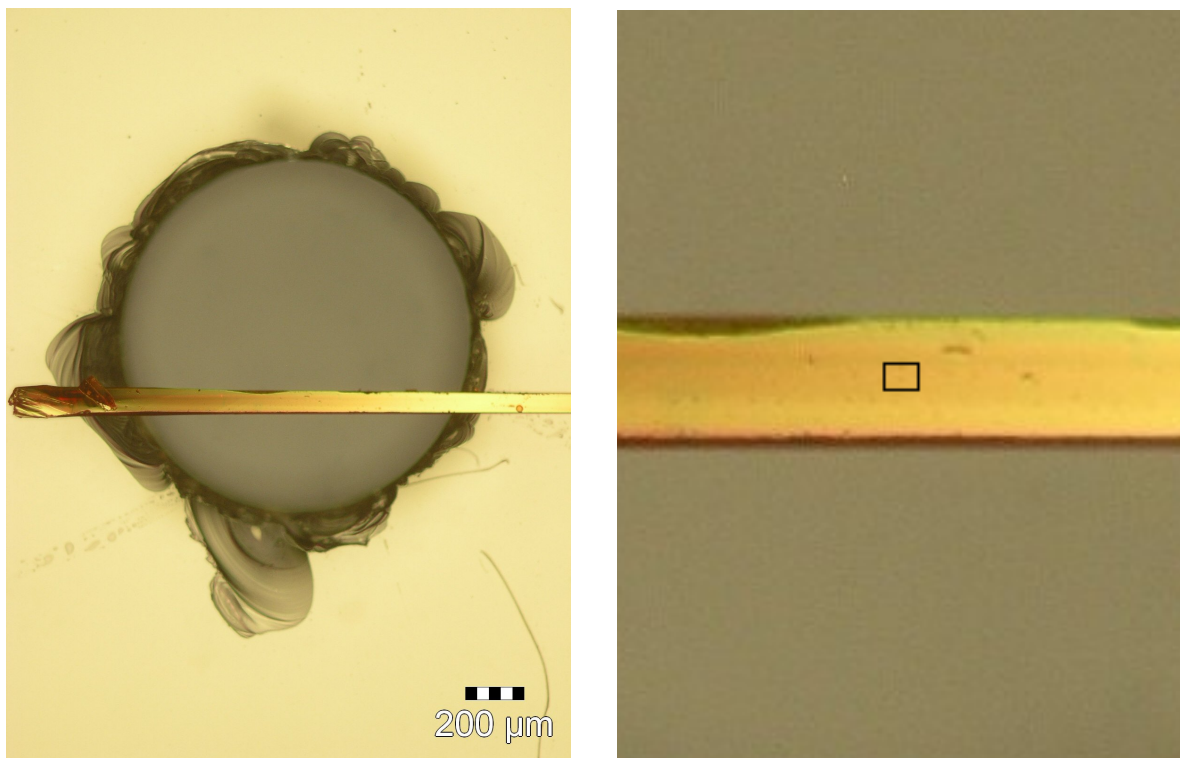


**Figure 3.33:** For transmittance measurements with the microscope the rubicene crystal is laid across a drilled hole on a glass substrate, as shown on the left. In the right image the area on the crystal surface, which is selected with the microscope's apertures to enable transmittance measurements, is marked.
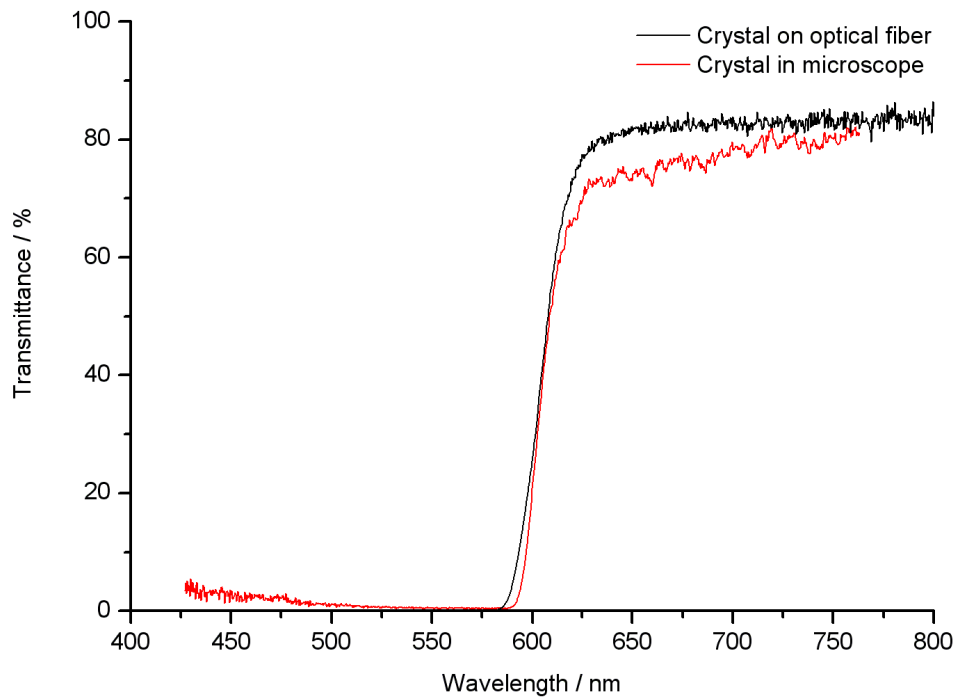
**Figure 3.34:** Transmittance spectra of two different rubicene crystals employing the measurement setup with the crystal attached to an optical fiber and the measurement setup with the microscope.

play a minor part the absorbance spectra represent the crystals' absorption properties. The absorption edge is located at approximately 600 nm in both spectra and provides an indication that the energy gap between the valence band and the conduction band of a rubicene crystal is about 2.07 eV.

### 3.5.2 Photoluminescence

As described in Section 3.4.3 photoluminescence originates from radiative transitions of photon-induced, excited electrons into the ground state in atoms or molecules. To determine the photoluminescence emission spectrum of a rubicene crystal a measurement setup with the IR-Plan infrared microscope, the MS125 spectrometer and a Brilliant Nd:YAG-laser from Quantel (Les Ulis, France), operated in pulsed mode (pulse duration: 4.5 ns, repetition rate: 10 Hz), was built. A scheme of this setup is illustrated in Figure 3.36. For excitation the crystal is illuminated with a directed, monochromatic laser beam. Since the laser uses a
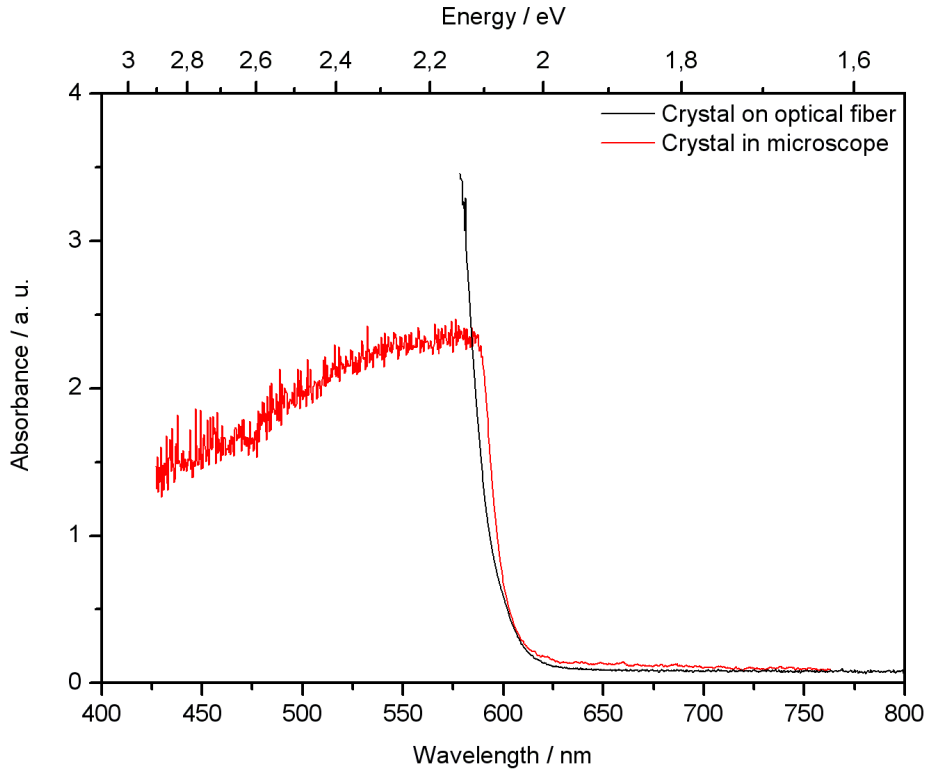
**Figure 3.35:** Absorbance spectra of two different rubicene crystals employing the measurement setup with the crystal attached to an optical fiber and the measurement setup with the microscope.

Nd:YAG-crystal as lasing medium it emits light with a wavelength of typically 1064 nm. To shift the wavelength of the emitted laser light into the crystal's absorption range the laser has to be operated with a special attachment containing a crystal with non-linear optical properties. As a consequence second harmonic generation (SHG) of the laser light occurs. This doubling of the laser light's frequency yields a wavelength of 532 nm which is completely within the crystal's absorption range. For examination the rubicene crystal is placed across a drilled hole on a glass substrate in the microscope again, equally to the transmittance measurements. The laser beam hits the crystal from the side in such a way that the beam's direction is nearly perpendicular to the microscope's optical axis. Hence the emission light from the crystal is measured almost perpendicular to the direction of the excitation light by the microscope's optics. In the end an optical fiber is used to guide the emission light from the microscope to the spectrometer. The light beam leaves the laser vertically polarized. However the beam's plane of polarization is rotated through 90° by the setup's reflectors and hence horizontally polarized light impinges on the rubicene crystal.
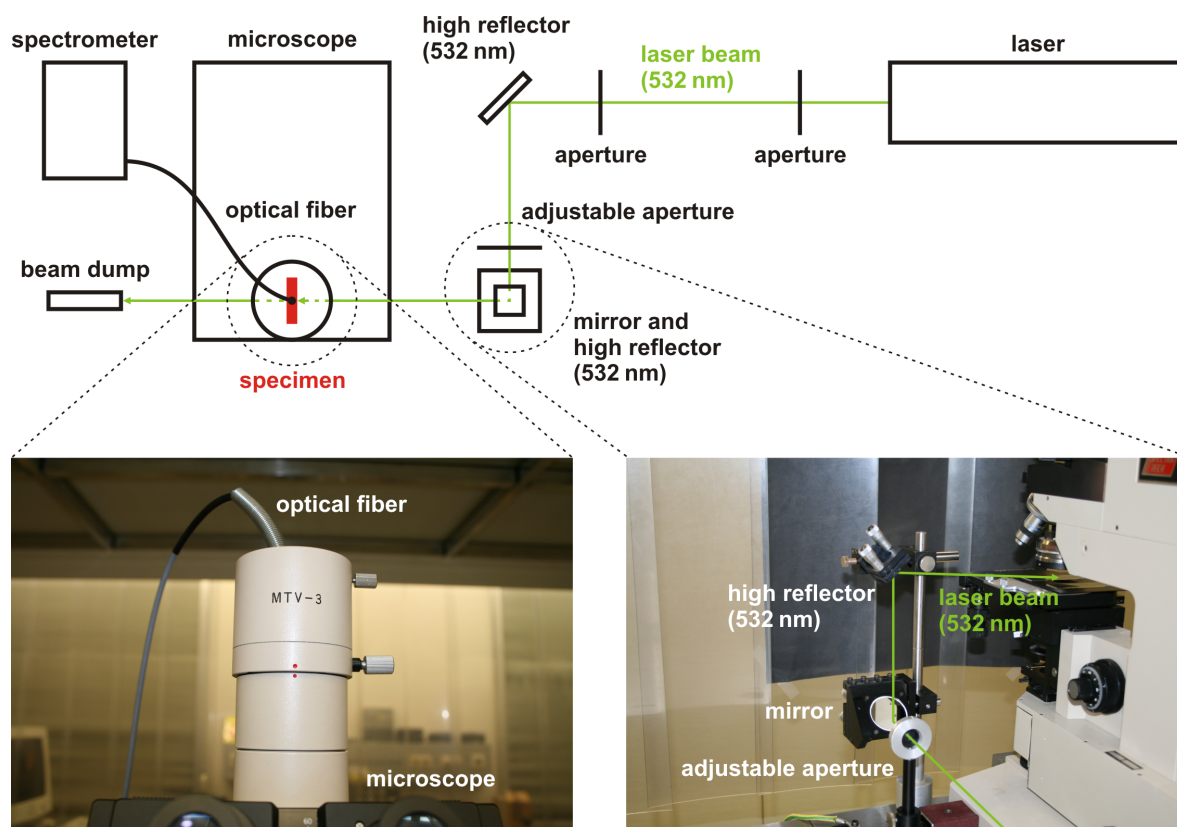
**Figure 3.36:** Setup for photoluminescence measurements of rubicene crystals, drawn schematically. High reflectors attuned to the laser light's wavelength (532 nm) are needed to filter out contributions from the flash light which is used as energy pump within the laser.

In Figure 3.37 the photoluminescence emission spectrum of a rubicene crystal, excited with light from the frequency-doubled Nd:YAG-laser, is visible. Additionally the crystal's absorbance spectrum is depicted too, proving that this laser light is adequate to excite a rubicene crystal. During measurements the laser's intensity has to be adjusted with reasonable care. Experience has shown that rough excitation with high intensity laser light can lead to degeneration or even destruction of the rubicene crystal, as illustrated in Figure 3.38.
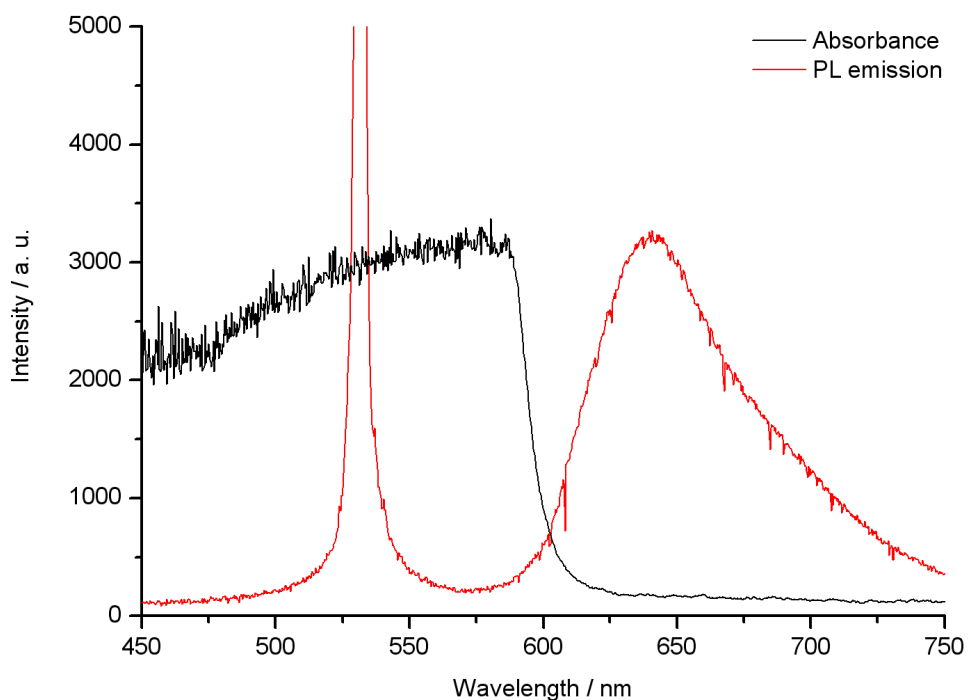
**Figure 3.37:** Absorbance spectrum and photoluminescence (PL) emission spectrum of a rubicene crystal. The peak at 532 nm results from laser stray light and, considering the absorbance spectrum, it demonstrates that light provided from a frequency-doubled Nd:YAG-laser is adequate to excite a rubicene crystal.
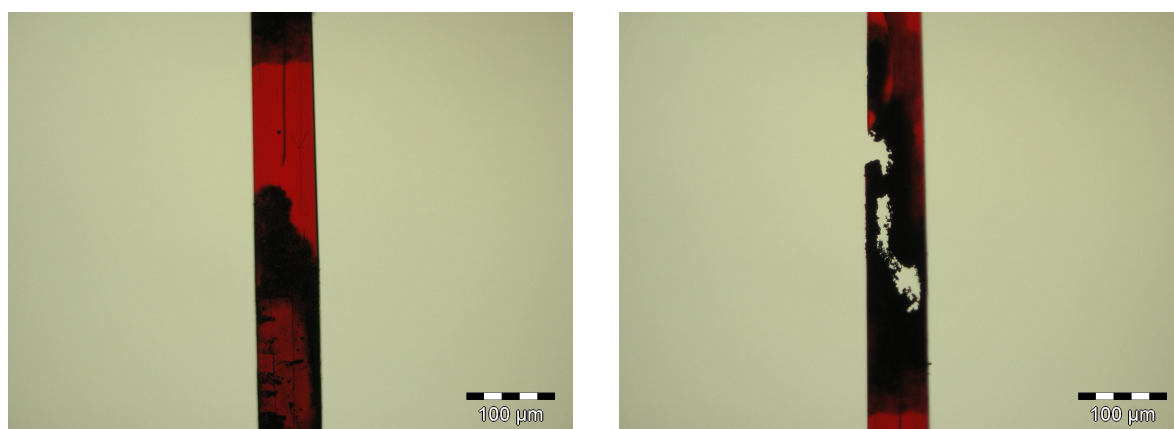


**Figure 3.38:** Damaged rubicene crystal after rough excitation with laser light. The left image shows a strongly degenerated area of the crystal, whereas the area on the right is already partly wrecked.

### 3.5.3 Electroluminescence

Electroluminescence is another excitation type for luminescence. In contrast to photoluminescence the energy needed to excite electrons isn't added by absorption of photons, but instead through an electric field induced by a voltage. A common way to achieve electroluminescence in organic semiconductors is the contacting with two materials of differently high work functions which serve as electrodes, most likely accomplished as thin metallic layers. Applying a voltage causes the high work function material to act as anode which injects holes into the valence band of the semiconductor. Contrary the low work function material is forced to inject electrons into the conduction band, thus being the cathode. Subsequently the injected electrons and holes attract each other by Coulomb forces and form bound states which are called excitons. The decay of an exciton generates a photon through the recombination process of electron and hole, resulting in electroluminescence emission.

Figure 3.39 evinces electroluminescence of a rubicene crystal, which is observed as a voltage of about $150 \, \mathrm{V}$ is applied to the crystal. In this simple setup the crystal is placed on a gold substrate. A tapered fine copper wire is used as tip to contact the crystal on top. For contacting a two-axis manipulator is used which facilitates a precise adjustment of the tip, necessary to avoid cracking of the rubicene crystal as it is contacted. Regarding the work functions of gold and copper, $5.10 \, \mathrm{eV}$ and $4.65 \, \mathrm{eV}$ (as stated by Michaelson [15]), respectively, the gold substrate is designated as anode and the copper tip as cathode.
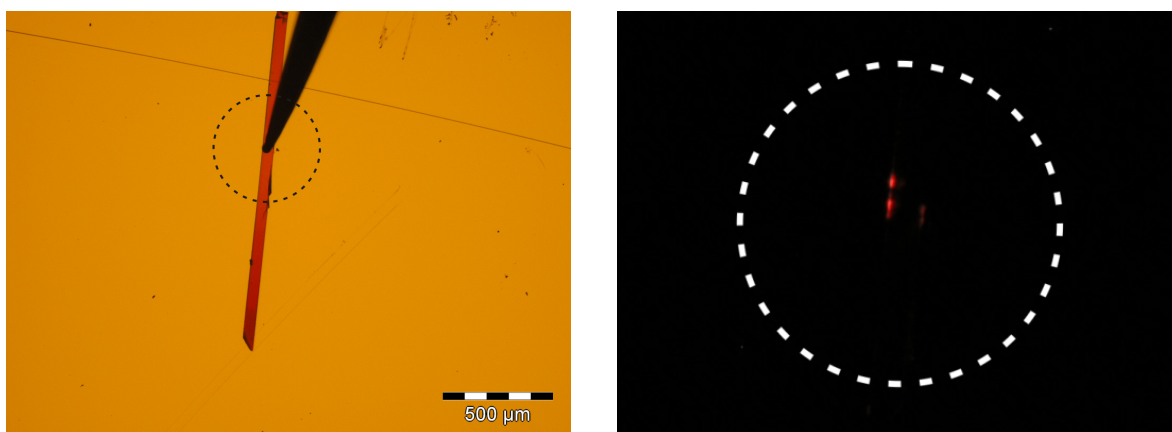


**Figure 3.39:** Electroluminescence featured by a rubicene crystal. In the left image one can see the crystal on a gold substrate, on top contacted with a fine copper tip. The image on the right shows an enlargement of the marked area where electroluminescence emission light comes from the rubicene crystal as a voltage of about $150 \, \mathrm{V}$ is applied between substrate and tip.

## 3.6 Surface Forced Growth

The growth of organic layers or films on various substrate surfaces becomes more and more important in the field of solid state physics. For organic laser devices the formation of homogeneous organic films is essential. However the realization of such homogeneous films is still a challenging task. For investigating the surface forced growth of rubicene different substrates are chosen. The fabrication is always based on a rubicene-toluene solution, regardless of the substrate. Film forming via slow solvent evaporation and dip coating are the two methods which are exerted. Since rubicene forms crystals instead of films on various substrates, as described in Sections 3.6.1.1 and 3.6.2.1, the surface forced growth of a dichromophoric perylene-derivative is investigated too, also by use of toluene as solvent.

Starting from the same rubicene powder as used for the growth of rubicene crystals with a purity of 98 %, a saturated rubicene-toluene solution is obtained in an analogous manner as described in Section 3.1.1.

Powder of the dichromophoric perylene-derivative, received from Langhals, was synthesized as described in [12]. Figure 3.40 presents the molecular structure of this dye. The perylene-derivative powder is dissolved in previously filtered (0.22 µm syringe filter) toluene (purity: $\geq 99.5\,\%$). The amounts of powder and toluene are controlled by the ALC electric precision balance and a scaled syringe, respectively. In doing so a perylene-derivative-toluene solution with a concentration of 3.55 mg/ml and another with a concentration of 0.01 mg/ml are achieved. The highly concentrated solution is used for the growth experiments, whereas the diluted solution is poured into a cleaned quartz cuvette to enable spectroscopic measurements with the RF-5301PC spectrofluorophotometer. Figure 3.41 depicts the obtained photoluminescence excitation and emission spectra of this perylene-derivative-toluene solution. It's evident that the solution's absorption edge is located at approximately 555 nm.
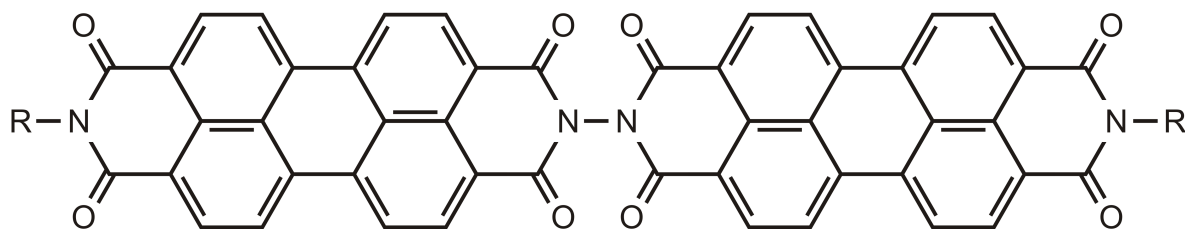


**Figure 3.40:** Illustration of a molecule of the dichromophoric perylene-derivative investigated (where the rest R is $CH(C_4H_9)_2$), reproduced from [12].
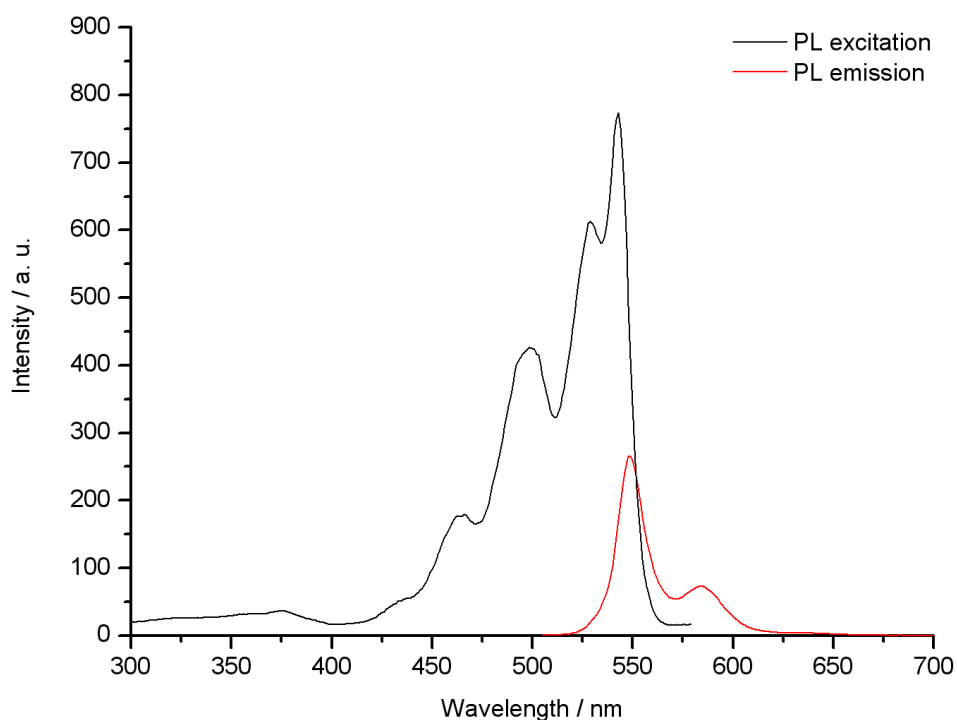
**Figure 3.41:** Photoluminescence (PL) excitation and emission spectra of a perylene-derivative-toluene solution (concentration: 0.01 mg/ml). The emission wavelength for the excitation spectrum is set to 584 nm. The excitation wavelength for the emission spectrum is 500 nm.

### 3.6.1 Film Forming via Solvent Evaporation

In this straightforward film growth method the substrate is immersed in a solution. Thereby the substrate is placed plane onto the bottom of a covered Petri dish containing the solution, with its surface upturned. As the solvent slowly evaporates the volume of the solution decreases and at a certain point the solution withdraws from the substrate's surface. However the solution's withdrawal from the surface isn't anywhere near as defined as in the process of dip coating, which is explained in Section 3.6.2. If there are slight surface irregularities the solution remains longer in troughs and lower surface areas than elsewhere, meaning that the thickness of the grown film is higher on such areas.

**3.6.1.1 Rubicene on Hydrogen-Terminated Silicon-(111) Surface**

For investigating the growth of rubicene on a hydrogen-terminated silicon-(111) surface a square piece of a silicon wafer (diameter: 100 mm, thickness: 525 μm), made by Silchem (Freiberg, Germany), is used. The orientation of this p-type (doped with boron) silicon wafer is (111). To obtain a hydrogen-terminated silicon-(111) surface the square piece of the wafer is chemically treated according to the following procedure, which is derivated from the process described by Sakaue et al. [18]:

1. Ultrasonic cleaning in acetone ($C_3H_6O$, purity: $\geq 99\,\%$) with a Transsonic T310/H ultrasonic cleaner from Elma (Singen, Germany) for 10 min and subsequent drying by a $CO_2$ gas flow

2. Immersion in chromic-sulfuric acid ($2\,\%$ $CrO_3$ in $H_2SO_4$) for 10 min

3. Thorough rinsing with distilled water and subsequent drying by a $CO_2$ gas flow

4. Immersion in a $5\,\%$ hydrofluoric acid ($HF_{(aq)}$) for 10 min

5. Immersion in a heated $40\,\%$ ammonium fluoride solution ($NH_4F_{(aq)}$, temperature: $73\,°C$) for 30 s

6. Thorough rinsing with distilled water and storage in distilled water until usage

7. Drying by a $CO_2$ gas flow just before usage

All vessels used during this treatment (glass vessels for the acetone, the chromic-sulfuric acid and the distilled water and polytetrafluoroethylene (PTFE) vessels for the hydrofluoric acid and the ammonium fluoride solution) as well as the Petri dish needed in the growth experiment for the saturated rubicene-toluene solution are previously cleaned as described in the following:

1. Immersion in chromic-sulfuric acid for 10 min

2. Thorough rinsing with distilled water and subsequent drying by a $CO_2$ gas flow

3. Heating in an oven (temperature: $80\,°C$) for 2 min (only for glass vessels)
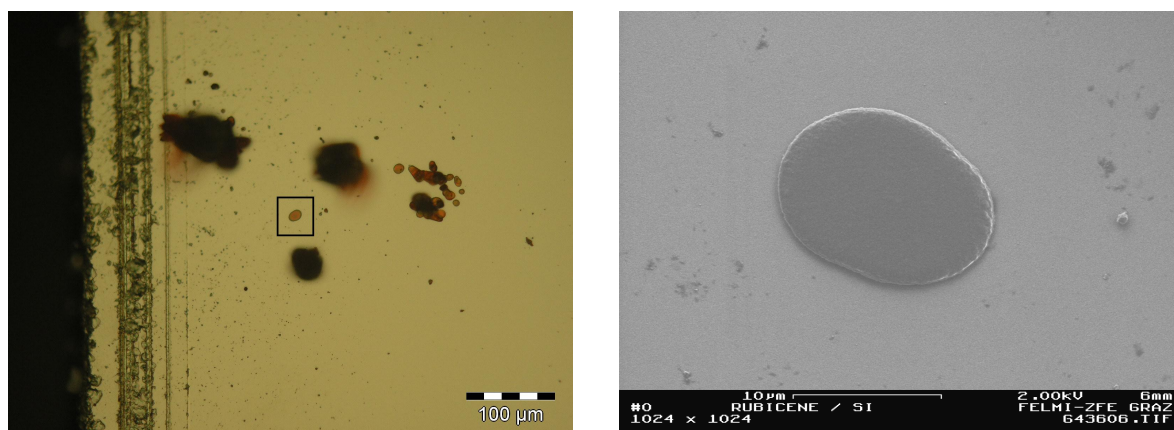
**Figure 3.42:** The left image illustrates small rounded rubicene layers, which are grown on a hydrogen-terminated silicon-(111) surface beside some bigger agglomerations of crystallized rubicene. On the right a SEM image of one of these rounded rubicene layers (the specific layer investigated with SEM is marked in the left image) is shown, indicating that they have very smooth surfaces.

As mentioned by Sakaue et al. [18] this preparation method yields a hydrogen-terminated silicon-(111) surface with a periodic terrace structure and very few atomic-scale defects. Such a well defined surface is expected to be a perfect substrate for fabrication of high-quality films and for applications in many other fields of research. The obtained hydrogen-terminated silicon-(111) surface is immersed in the saturated rubicene-toluene solution. After the evaporation of all the solvent there isn't any rubicene film grown on the surface, but instead one can find very flat rounded rubicene layers with diameters of the order of several μm, as depicted in Figure 3.42. In addition a SEM image of one of these rounded rubicene layers proves their surface smoothness. In Figure 3.43 a number of rubicene crystals are visible on the hydrogen-terminated silicon-(111) surface, which are highly branched as evinced in the corresponding SEM image. Moreover Figure 3.44 shows a rather large rubicene crystal without branches on the hydrogen-terminated silicon-(111) surface. In contrast to the crystal growth experiments from a rubicene-toluene solution, described in Section 3.1.4, this crystal exhibits some kind of structure on its surface. A supplemental SEM image of the crystal surface enables a closer look on this structure. All SEM images were recorded with the Gemini DSM 982 SEM.

### 3.6.2 Film Forming via Dip Coating

Dip coating is a process where a substrate is dipped into a solution and subsequently vertically withdrawn at a slow, constant speed. In order to grow reasonable films the substrate has to be clean and its surface should be quite smooth. The substrate's wettability is also of vital
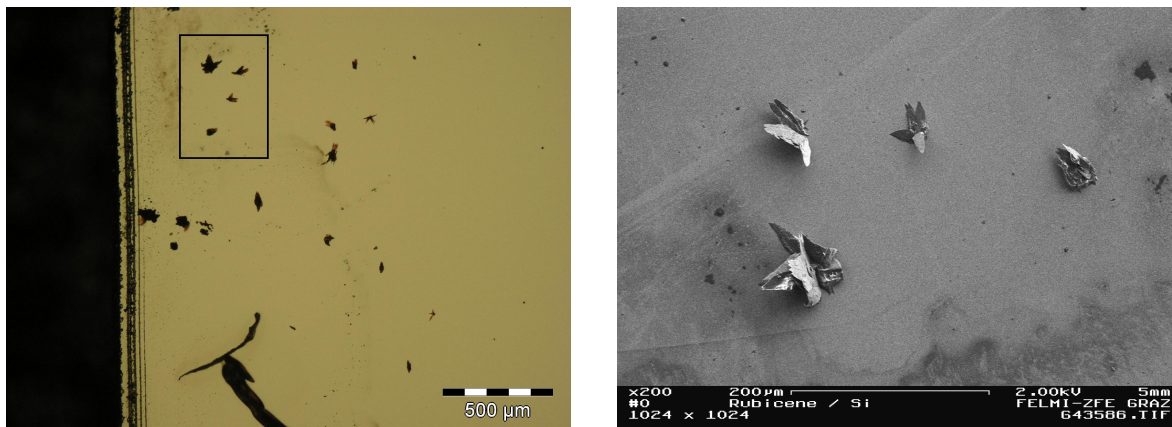
**Figure 3.43:** On the left several highly branched rubicene crystals can be noticed on the hydrogen-terminated silicon-(111) surface. Those crystals marked in the left image are also depicted in the SEM image on the right. As one can clearly see the crystals' branches are quite cultrate.
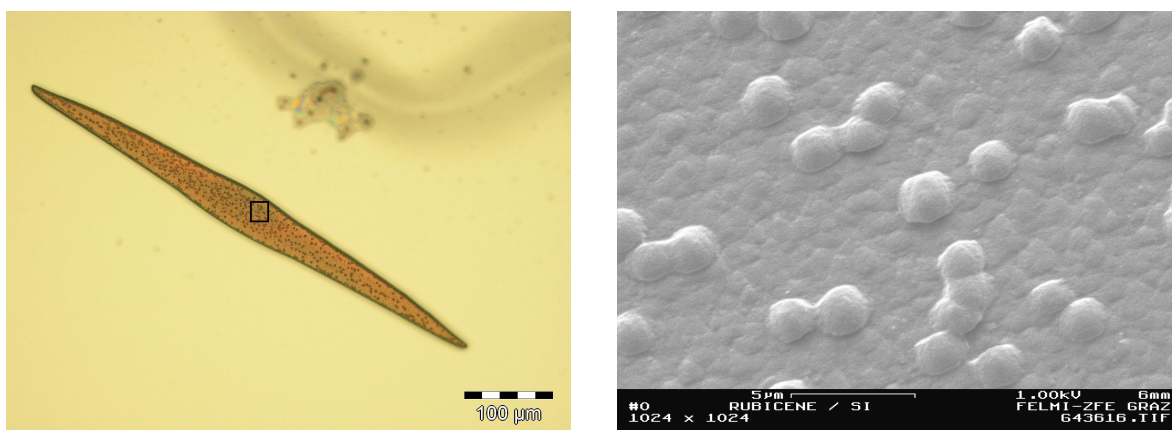


**Figure 3.44:** In the left image one can see a rubicene crystal grown on the hydrogen-terminated silicon-(111) surface. The structure on the crystal surface is displayed in the SEM image on the right. Additionally the area of the crystal surface which corresponds to this SEM image is marked in the left image.

importance since it encourages the formation of the meniscus, a thin wetting film reaching from the liquid's surface upwards the substrate. The evaporation of the solvent at the solution-substrate-air contact line on top of the meniscus causes the film growth as the substrate is pulled out of the solution. Molecules of the material dissolved in the solution remain on the just dried surface area of the substrate and molecules in the solution are transferred towards the meniscus' top, altogether resulting in a film on the substrate. In general a slower withdrawal speed can be associated with thicker films and vice versa.

The dip coating experiments were carried out on a NANO DIP ND-0407 dip coater from SDI Company, Ltd. (Kyoto, Japan). This dip coater is capable of lifting its substrate holder at a very constant speed, adjustable from $10\,nm/s$ up to $2\,mm/s$. Furthermore its overall stroke distance is $50\,mm$. An additional perspex box is put over the dip coater to protect from any external air flow during the dip coating process.

### 3.6.2.1 Rubicene on Glass Surface

Before dip coating the glass substrate is chemically treated to obtain a hydrophilic glass surface and thus enhance its wettability, according to the following procedure:

1. Cleaning with isopropyl alcohol and subsequent drying by a $CO_2$ gas flow

2. Immersion in chromic-sulfuric acid for $10\,min$

3. Thorough rinsing with distilled water and storage in distilled water

4. Ultrasonic cleaning in distilled water with the Transsonic T310/H ultrasonic cleaner for $10\,min$

5. Ultrasonic cleaning in filtered ($0.45\,\mu m$ syringe filter), distilled water with the Transsonic T310/H ultrasonic cleaner for $10\,min$

6. Storage in filtered ($0.45\,\mu m$ syringe filter), distilled water until usage

7. Drying by a $CO_2$ gas flow just before usage

All glass vessels, which are used for the distilled water during this procedure, are previously cleaned with isopropyl alcohol too. Dip coating of a so prepared glass substrate in the
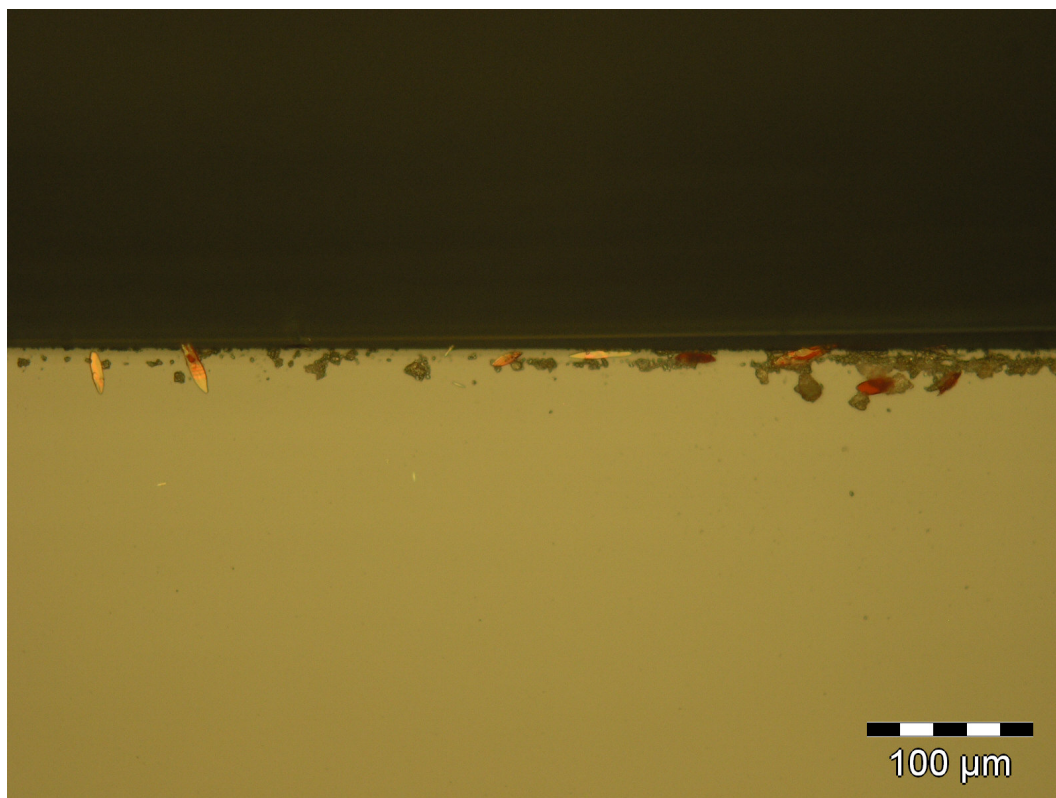
**Figure 3.45:** Rubicene crystals grown on scratches near the edge of a glass substrate in the course of dip coating in a saturated rubicene-toluene solution.

saturated rubicene-toluene solution at a speed of $500\,\mathrm{nm/s}$ doesn't lead to a rubicene film on the glass surface, but instead tiny rubicene crystals are grown on scratches on the surface, mainly located near the substrate's edge. The crystals can be seen in Figure 3.45. However there is no rubicene noticeable on the smooth areas of the glass surface.

### 3.6.2.2 Perylene-Derivative on Glass Surface

For investigating the growth of the dichromophoric perylene-derivative on glass surfaces a glass substrate is chemically treated in the same way as mentioned in Section 3.6.2.1. Then the prepared glass surface is dipped into the perylene-derivative-toluene solution with a concentration of $3.55\,\mathrm{mg/ml}$. Subsequent dip coating at a speed of $5\,\mathrm{\mu m/s}$ produces a very thin perylene-derivative film on the glass surface, even though the film isn't very homogeneous, as shown in Figure 3.46. Moreover there are certain stripes where the film is interrupted, most likely due to sudden vibrations during dip coating accompanied by a drop of the solution's meniscus. Additionally one can see very small, dark dots which are agglomerations
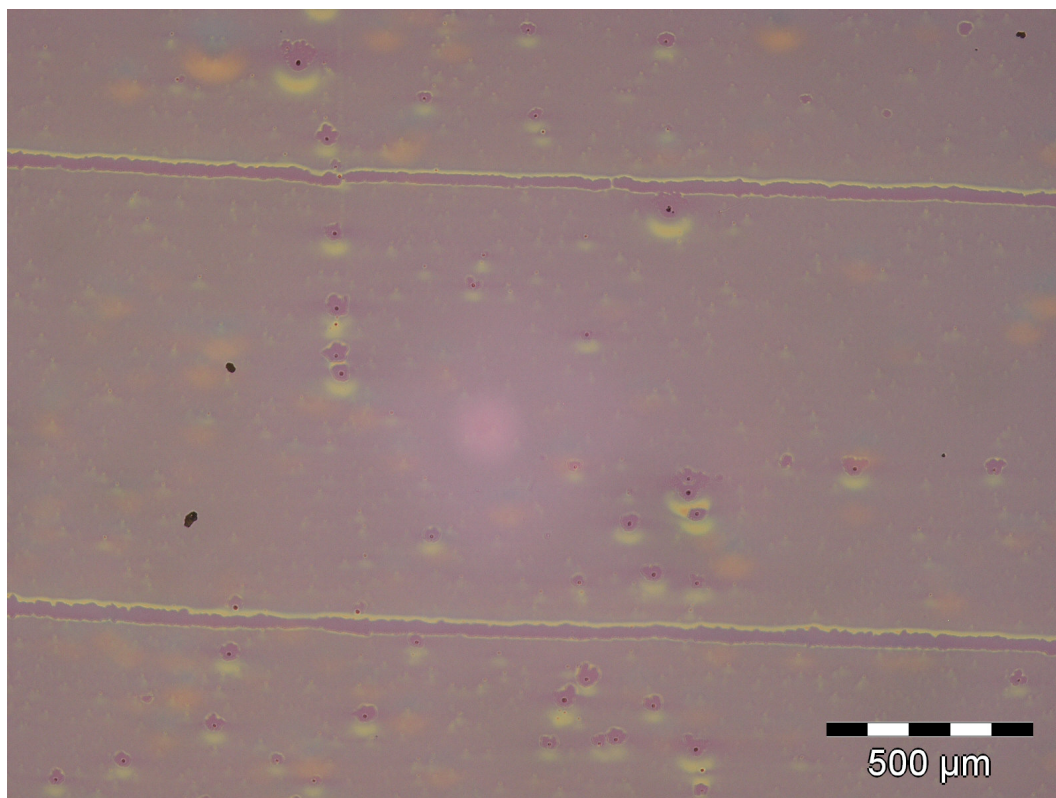
**Figure 3.46:** Thin perylene-derivative film grown on a glass surface. The pink spot in the middle originates from reflections on the glass substrate, caused by the illumination light of the microscope (BX51 light microscope from Olympus, Tokyo, Japan).

of crystallized perylene-derivative. Around these agglomerations there are depleted areas in the perylene-derivative film because the perylene-derivative is gathered within the agglomerations.

### 3.6.2.3 Perylene-Derivative on Gold Surface

A piece of a silicon wafer which is coated with gold serves as substrate to investigate the growth of the dichromophoric perylene-derivative on gold surfaces. Before dip coating the gold substrate is immersed in toluene (purity: $\geq 99.5\,\%$) and treated with the ultrasonic cleaner for 10 min. Thereafter the substrate is dried by a $CO_2$ gas flow. Figure 3.47 shows a perylen film grown on the gold surface after dip coating with 1 µm/s in the perylene-derivative-toluene solution (concentration: 3.55 mg/ml). Equal to the perylene-derivative film grown on the glass surface agglomerations of crystallized perylene-derivative are also visible in this film. In addition to it the agglomerations are arranged in a pattern of more or less aligned stripes
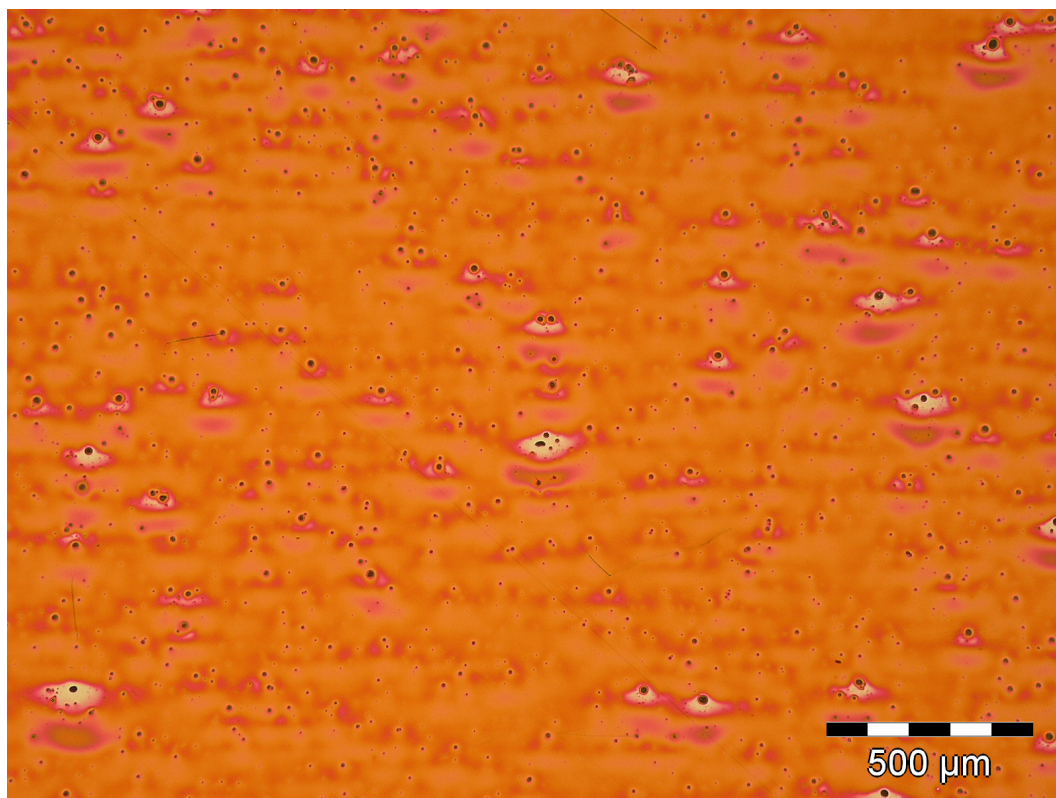
**Figure 3.47:** Perylene-derivative film grown on a gold surface. Due to influences of external vibrations the agglomerations of crystallized perylene-derivative in the film show a streaky pattern.

which is assumed to stem from the influence of external vibrations. To minimize the effect of these vibrations on the perylene-derivative film another dip coating experiment with the dip coater standing on a massive granite slab is accomplished, again at a speed of $1\,\mu m/s$. The granite slab, which is auxiliary stored on foam stripes, helps to supress vibrations from the ground. Furthermore the perspex box of the dip coater is cloaked with laboratory coats to prevent the whole setup from airborne vibrations. In Figure 3.48 the result of this dip coating experiment is depicted. It's evident that the agglomerations of crystallized perylene-derivative are distributed statistically now. The streaky pattern is completely gone, proving that this dip coating setup protects effectively against any external vibrations. Figure 3.49 illustrates the photoluminescence emission which occurs from this perylene-derivative film as it is illuminted from the side with a laser pointer providing light of $405\,nm$ wavelength. It's obvious that the light is rather emitted from the agglomerations of crystallized perylene-derivative than from the film.
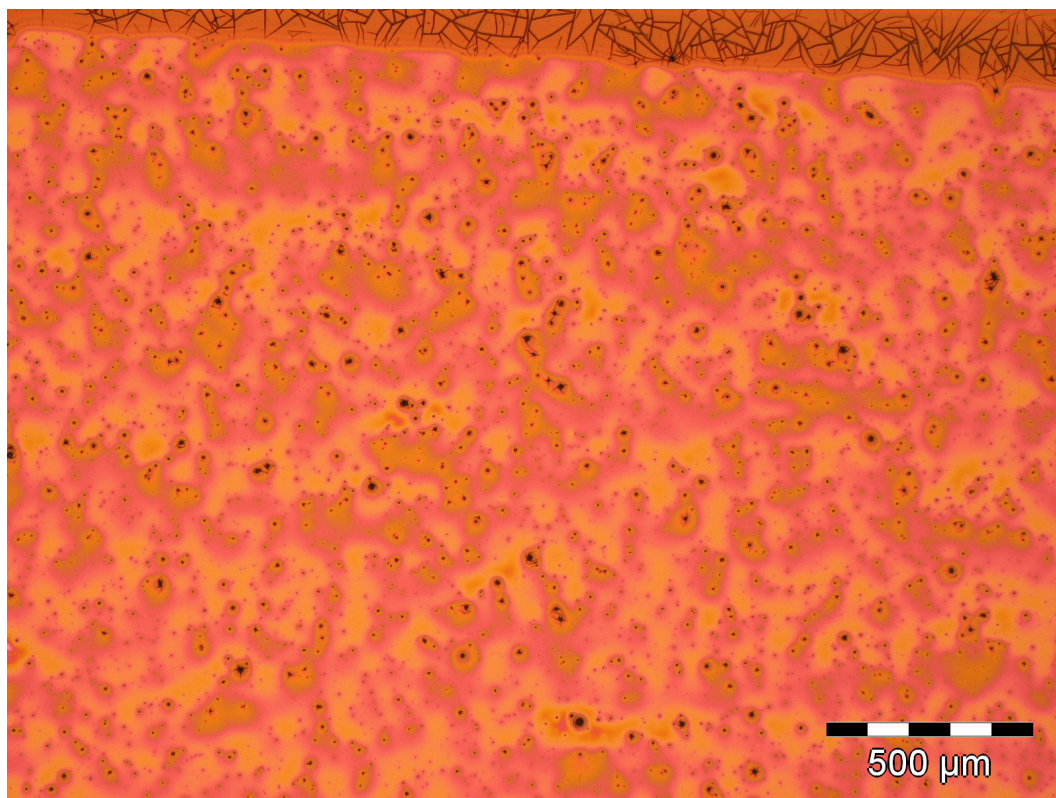
**Figure 3.48:** Perylene-derivative film grown on a gold surface without influences of external vibrations. On top, near the end of the substrate, the film is very thick and hence it is cracked.
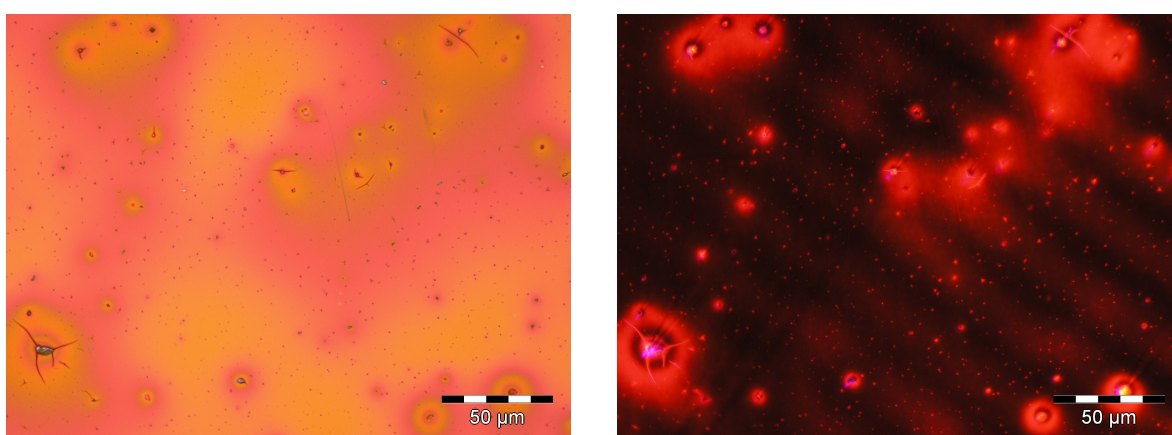


**Figure 3.49:** The left image depicts a certain area of the perylene-derivative film grown on the gold surface. In the right image photoluminescence emission occurring from this area is shown. Moreover there is a pattern of broad stripes slightly visible on the film. This pattern indicates waveguiding of the emission light within the film.

# 4  Outlook

## 4.1  Crystal as Optical Resonator

The basic knowledge of this section is deduced from [11, 22]. A simple type of an optical resonator consists of two facing mirrors, usually one high reflector and one partial reflector for output coupling of the light, and is used in lasers to form standing light waves within the gain medium. Light in the resonator is reflected many times from the mirrors and thus standing waves occur due to constructive interference of opposed light beams. The condition to be fulfilled is that the light's optical path within the resonator is an integer multiple of half its wavelength. Such constructive interfering light waves are called resonant. Accordingly non-resonant waves are suppressed through destructive interference. Consequently the energy of the electromagnetic field can only be deployed to several vibrational modes of the resonator, so called resonator modes, which correspond to the standing light waves. It now appears that a sufficient energy density, which is a necessary condition for stimulated emission to become more probable than spontaneous emission in the gain medium and thus inducing light amplification and laser operation, is just achieved for resonator modes.

Basically a simple plane parallel plate can be regarded as an optical resonator too. If the reflectivity of the plate's surfaces is high enough multiple beam interference appears as the plate is illuminated with light. In the case of constructive interference a standing wave of high intensity forms within the plane parallel plate, just like in an optical resonator. Considering its shape a rubicene single crystal excellently represents such a plane parallel plate. Moreover the crystal surfaces are very smooth, as demonstrated by the AFM measurements noticed in Section 3.2.2.1, and can be used as reflectors. The fairly different refractive indices between semiconductor materials like rubicene and the surrounding medium, generally air, provides for a certain reflectivity of the crystal surfaces.

### 4.1.1 Multiple Beam Interference

If a light beam impinges on a plane parallel plate of high reflectivity most of the beam's intensity is reflected back. The light beam which penetrates the plate has considerably less intensity. However this beam stays within the plate for many subsequent reflections because each time only a little fraction of the light can leave the plate, whereas most of the beam's intensity is reflected back from the plate's surfaces. This means that many light beams of nearly the same intensity leave the plate on both sides, resulting in multiple beam interference on each side. Assuming that there aren't any absorption losses within the plate both interference patterns, the one reflected back from the plate and the one occurring from light that passed through the plate, are complementary. In the case of destructive interference in reflection constructive interference occurs in transmittance and, as a result of energy conservation, the whole intensity can pass through the plane parallel plate. The reflected amount $I_R$ and the traversed amount $I_T$ of the incident light's intensity $I_0$ depend on the phase difference $\Delta\phi$ between two consecutive light beams and are determined by Airy's formulas:

$$I_R = I_0 \frac{(\frac{2F}{\pi})^2 \sin^2(\frac{\Delta\phi}{2})}{1 + (\frac{2F}{\pi})^2 \sin^2(\frac{\Delta\phi}{2})} \tag{4.1}$$

$$I_T = I_0 \frac{1}{1 + (\frac{2F}{\pi})^2 \sin^2(\frac{\Delta\phi}{2})} \tag{4.2}$$

From these equations one can obtain the corresponding reflection and transmittance curves of the plane parallel plate. $F$ is the so called finesse, which is defined as follows:

$$F = \frac{\Delta\tilde{\nu}_{FSR}}{\delta\tilde{\nu}} \tag{4.3}$$

Thereby $\delta\tilde{\nu}$ is the full width at half maximum of the peaks in the transmittance curve in wavenumber units and the quantity $\Delta\tilde{\nu}_{FSR}$ is the free spectral range, the spacing between adjacent transmittance peaks in wavenumber units. Therefore a higher finesse means sharper transmittance peaks. If the light impinges perpendicular on the plate the free spectral range is given by the refractive index $n$ and the thickness $d$ of the plate:

$$\Delta\tilde{\nu}_{FSR} = \frac{1}{2nd} \tag{4.4}$$

For the finesse the following expression, which only depends on the reflectivity $R$ of the plate's surfaces, can be calculated:

$$F = \frac{\pi\sqrt{R}}{1 - R} \tag{4.5}$$
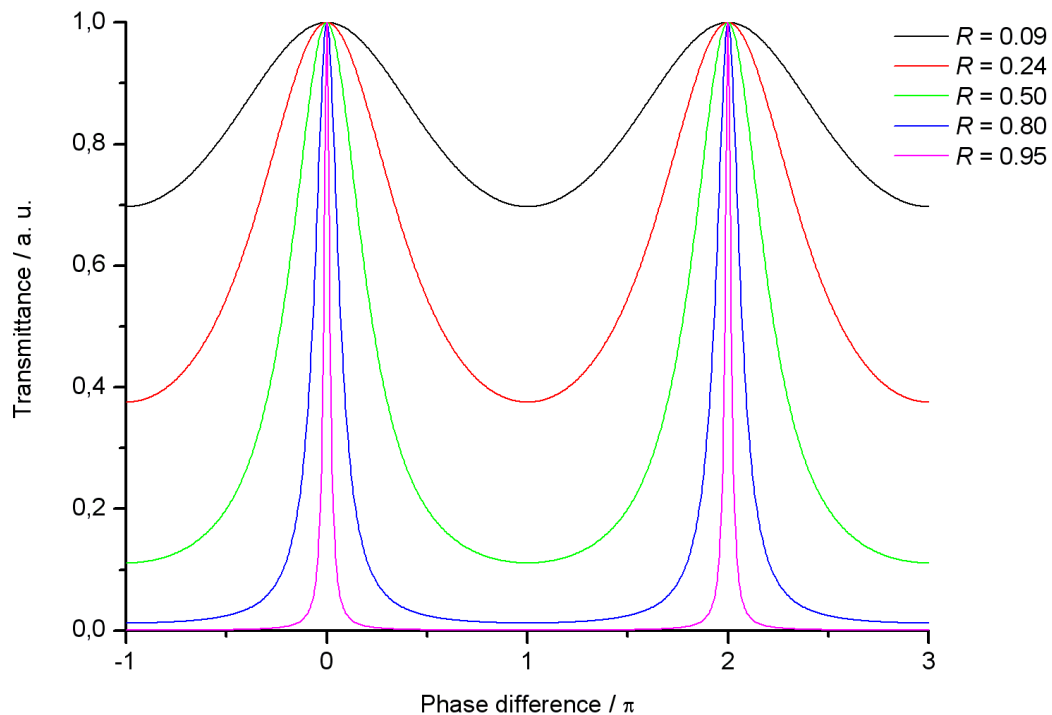
**Figure 4.1:** Transmittance curves of a plane parallel plate for different reflectivity values.

Figure 4.1 shows transmittance curves of a plane parallel plate for various reflectivity values of the plate's surfaces as a function of the phase difference between two consecutive light beams, according to Equations 4.2 and 4.5. It can be seen from this curves that higher reflectivities, and thus higher finesse values, lead to sharper transmittance peaks. These peaks represent the resonator modes of the plane parallel plate.

To visualize the transmittance peaks of a rubicene crystal the MS125 spectrometer was used. This time, contrary to the transmittance measurements described in Section 3.5.1, the spectrometer is used with a grating with 2400 lines/mm to enhance the spectrometer's resolution. The crystal is placed across a tiny hole on an aluminum foil in a way that it fully covers the hole. Then the foil, together with the crystal, is attached to an optical fiber so that the foil's hole matches the entrance window in the middle of the optical fiber. This setup ensures that only light which traversed through the rubicene crystal is collected by the optical fiber. Subsequently the crystal is illuminated from above with light of an ordinary bulb, which in addition is polarized with a linear polarizer. Two spectra of light which passed through the crystal are measured with the optical fiber and the spectrometer, one with the
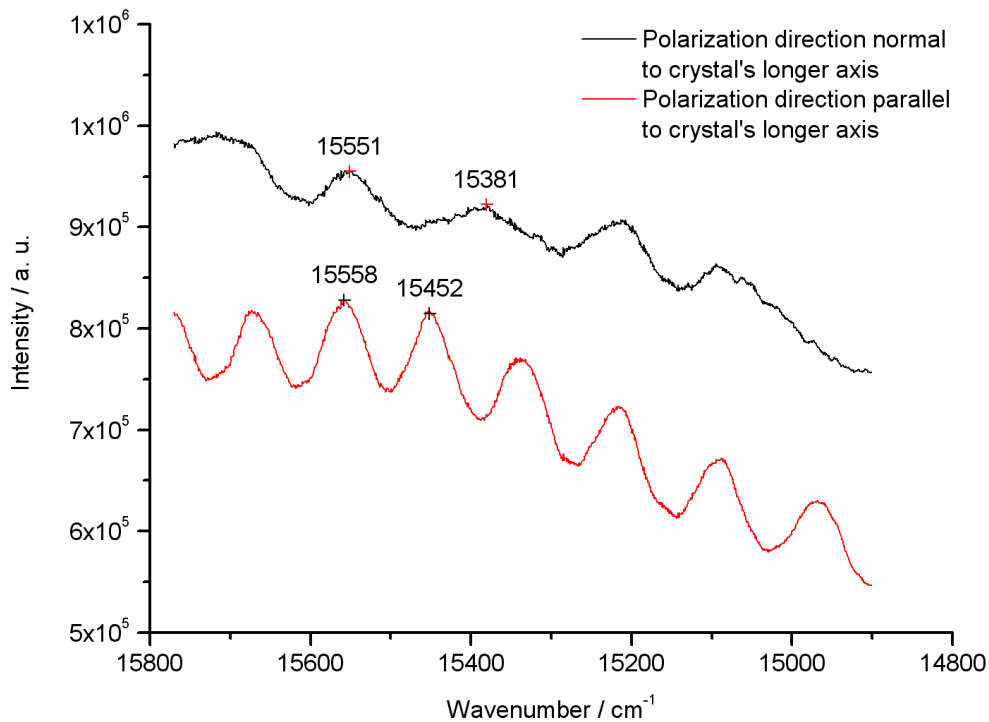
**Figure 4.2:** Transmittance curves of a rubicene crystal for different polarization directions of the incident light. The curves aren't corrected for the spectrum of the bulb's light.

light's polarization direction being normal to the crystal's longer axis and one with the light's polarization direction being parallel to it. These spectra are depicted in Figure 4.2. From two adjacent transmittance peaks the free spectral range can be determined for the normal and the parallel polarization direction:

$$\Delta\tilde{\nu}_{FSR, \ normal} = 170\,\mathrm{cm}^{-1}$$
$$\Delta\tilde{\nu}_{FSR, \ parallel} = 106\,\mathrm{cm}^{-1}$$

### 4.1.1.1 Crystal Refractive Indices

Figure 4.3 shows the rubicene crystal on the aluminum foil, viewed from the side. From this image the thickness of the crystal is estimated to be $(16 \pm 2)\,\mathrm{\mu m}$. Assuming that the light impinges perpendicular on the crystal surface the refractive indices for both polarization
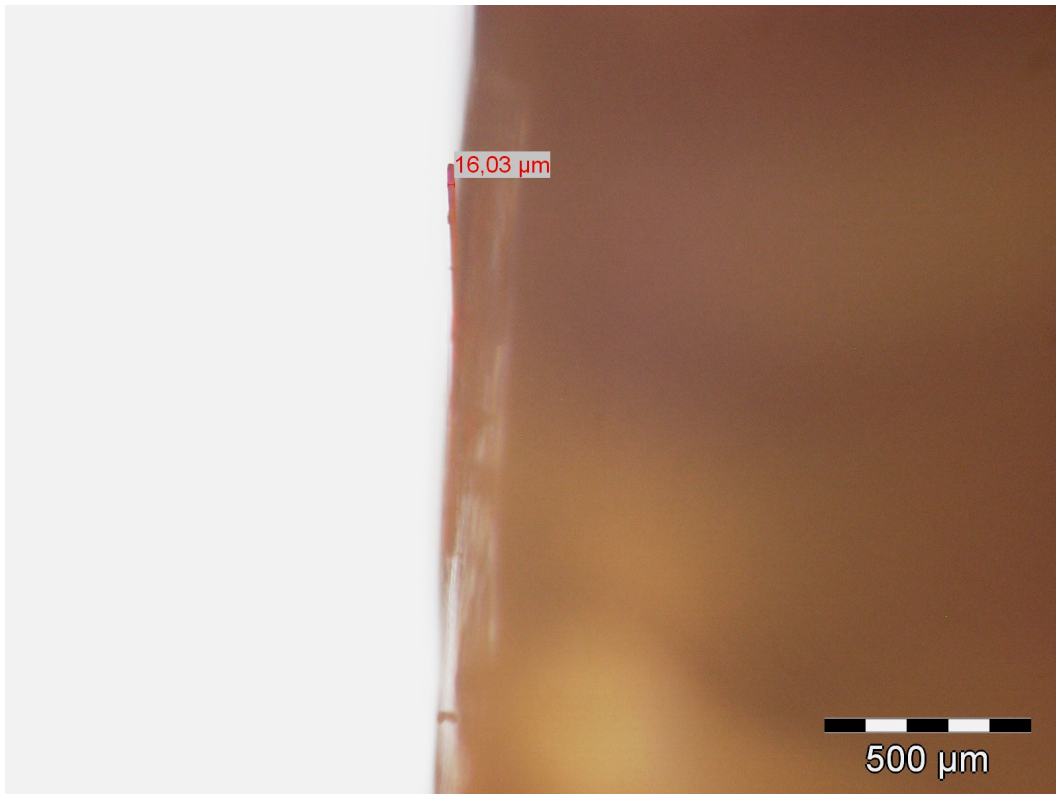
**Figure 4.3:** Side view on the rubicene crystal which is placed across a tiny hole on the aluminum foil. The thickness of the crystal is measured with the aid of the light microscope's software.

directions can be calculated from the free spectral ranges and the crystal's thickness by Equation 4.4:

$$n_{normal} = 1.8 \pm 0.2$$
$$n_{parallel} = 2.9 \pm 0.4$$

The errors of these and the subsequent calculated quantities are evaluated via error propagation, using the method of partial derivatives. The results above clearly reveal the birefringent character of the rubicene crystal.

### 4.1.1.2 Crystal Surface Reflectivities

Furthermore the refractive indices of the surrounding medium (air, $n_1 \approx 1$) and the crystal ($n_2$, see above) yield the reflectivity of the crystal surface in case of perpendicular incidence

of light, according to the following equation:

$$R = \left(\frac{n_2 - n_1}{n_2 + n_1}\right)^2 \tag{4.6}$$

In this way the following reflectivity values of the crystal surface are obtained, one for light being normal polarized to the crystal's longer axis and one for light being parallel polarized to this axis:

$R_{normal} = 0.09 \pm 0.03$
$R_{parallel} = 0.24 \pm 0.05$

For comparison the transmittance curves of plane parallel plates with these reflectivity values are shown in Figure 4.1 too. From the corresponding transmittance peaks it's evident that the results of the rubicene crystal investigated aren't good enough to apply the crystal as optical resonator. In order to use a rubicene single crystal as an optical resonator with distinct resonator modes, for instance in lasers, the reflectivity of the crystal surfaces has to be enhanced adequately. This can be achieved with dielectric multi layers on the crystal surfaces, if only possible for small spectral ranges.

# 5 Conclusion

In this master thesis the organic semiconductor rubicene was investigated with respect to its physical and photophysical properties.

The growth of rubicene crystals from solutions was demonstrated with various organic solvents, namely cyclohexanone, chlorobenzene and toluene. Considering all solvents the best results were achieved with a rubicene-toluene solution, yielding rubicene single crystals of acceptable quality. Therefore just crystals grown from the rubicene-toluene solution were further analyzed.

The grown rubicene crystals were examined regarding their surface topography and chemical composition. SEM measurements as well as AFM measurements clearly evinced a layered terrace structure on the quite smooth crystal surfaces. With the aid of AFM a very low root mean squared surface roughness between $0.4\,\text{Å}$ and $0.7\,\text{Å}$ was found. Moreover EDXS analyses of a crystal didn't show any considerable impurities arising from the growth process within the crystal since mainly carbon was detected, as it was expected. IR spectra of several grown crystals were obtained in the course of FTIR spectroscopy. The results showed that there were rubicene crystals of high chemical purity, which was indicated by the absence of absorption peaks arising from saturated hydrocarbons. Nevertheless FTIR spectroscopy also evinced that not all grown crystals were chemically that pure. Therefore a characterization and selection of grown rubicene crystals via FTIR spectroscopy is very important.

Applying XRD the structures of several rubicene crystals were determined. The results were the same for all crystals and indicated the crystal structure to be monoclinic. Furthermore the corresponding lattice type could be identified as primitive monoclinic Bravais lattice. Beside the dimensions of the unit cell the intramolecular distances of the packed rubicene molecules were examined too. Additionally the XRD measurements provided the distance of two adjacent parallel molecules in a rubicene crystal. The value found is very small compared to that of other organic crystals.

Spectroscopic investigations in the visible and ultraviolet spectral range of rubicene molecules

in a toluene solution were performed in terms of transmittance measurements and the recording of photoluminescence excitation and emission spectra. In doing so an energy gap of about 2.25 eV between HOMO and LUMO of a rubicene molecule was obtained. Regarding this value one has to take the dielectric surrounding of the molecules, due to the solvent, into account.

The grown rubicene crystals were also spectroscopically investigated, employing transmittance measurements with visible light and photoluminescence emission measurements which were induced by laser excitation. The energy gap between the valence band and the conduction band of a rubicene crystal was evaluated to be about 2.07 eV. The obvious difference between the energy gap of rubicene molecules in solid state and that of rubicene molecules in solution would have to be investigated in further experiments. Moreover it was possible to demonstrate electroluminescence emission light coming from a crystal as a rather high voltage was applied.

The surface forced growth of rubicene on different substrates was accomplished via the method of evaporating the solvent from rubicene-toluene solutions and the process of dip coating. In addition to it a dichromophoric perylene-derivative was grown on various surfaces too.

Finally the capability of a rubicene single crystal to be used as optical resonator was inspected. From the peaks in the crystal's transmittance spectra, which were recorded with an adequate resolution, the refractive indices and thus the reflectivities of the smooth crystal surfaces could be calculated for two polarization directions of the impinging light. The higher refractive index of $2.9 \pm 0.4$ (determined in the wavelength range between 642.8 nm and 647.2 nm), which was observed for light being parallel polarized to the crystal's longer axis, yields a reflectivity of $0.24 \pm 0.05$. Although these values aren't much lower than those of the organic single crystal presented by Yamao et al. [24] ($n = 4.0$, $R = 0.36$), which features laser oscillations as it is optically pumped, it turned out that the obtained reflectivity value is still too low for an optical resonator of good quality. However a significant reflectivity enhancement might be achieved via dielectric multi layers on the crystal surfaces.

# Bibliography

[1] L. Bergmann and C. Schäfer. *Lehrbuch der Experimentalphysik - Band 6 Festkörper.* Walter de Gruyter, 2nd edition, 2005.

[2] Y. Chen, Z. Li, Z. Zhang, D. Psaltis, and A. Scherer. Nanoimprinted circular grating distributed feedback dye laser. *Applied Physics Letters*, 91(5):051109, 2007.

[3] C. Cohen-Tannoudji, B. Diu, and F. Laloë. *Quantum Mechanics - Volume 2.* Wiley-Interscience, 2nd edition, 1977.

[4] F. A. Cotton and G. Wilkinson. *Advanced Inorganic Chemistry.* Wiley, 5th edition, 1988.

[5] F. Ehlotzky. *Quantenmechanik und ihre Anwendungen.* Springer, 2005.

[6] W. Grogger. *Rasterelektronenmikroskopie.* Lecture notes, TU Graz, 2008.

[7] M. Hesse, H. Meier, and B. Zeeh. *Spektroskopische Methoden in der organischen Chemie.* Georg Thieme, 7th edition, 2005.

[8] O. D. Jurchescu, A. Meetsma, and T. T. M. Palstra. Low-temperature structure of rubrene single crystals grown by vapor transport. *Acta Crystallographica Section B*, 62(2):330–334, 2006.

[9] C. Karnutsch, M. Stroisch, M. Punke, U. Lemmer, J. Wang, and T. Weimann. Laser Diode-Pumped Organic Semiconductor Lasers Utilizing Two-Dimensional Photonic Crystal Resonators. *IEEE Photonics Technology Letters*, 19(10):741–743, 2007.

[10] G. Kranzelbinder and G. Leising. Organic solid-state lasers. *Reports on Progress in Physics*, 63(5):729–762, 2000.

[11] H. Kuzmany. *Festkörperspektroskopie - Eine Einführung.* Springer, 1990.

[12] H. Langhals and W. Jona. Intensiv-Farbstoffe durch Chromophor-Chromophor-Wechselwirkungen: di- und trifluorophore Perylen-3,4:9,10-bis(dicarboximide). *Angewandte Chemie*, 110(7):998–1001, 1998.

[13] R. Li, W. Hu, Y. Liu, and D. Zhu. Micro- and Nanocrystals of Organic Semiconductors. *Accounts of Chemical Research*, 43(4):529–540, 2010.

[14] M. Lu, S. S. Choi, U. Irfan, and B. T. Cunningham. Plastic distributed feedback laser biosensor. *Applied Physics Letters*, 93(11):111113, 2008.

[15] H. B. Michaelson. The work function of the elements and its periodicity. *Journal of Applied Physics*, 48(11):4729–4733, 1977.

[16] V. Sachweh and H. Langhals. Synthese von Reinst-Rubicen und Rubicen-Derivaten. *Chemische Berichte*, 123(10):1981–1987, 1990.

[17] H. Sakata and K. Natsume. Distributed-feedback vertical cavity structures for optically pumped solid-state organic lasers. *Optical and Quantum Electronics*, 39(7):577–583, 2007.

[18] H. Sakaue, S. Fujiwara, S. Shingubara, and T. Takahagi. Atomic-scale defect control on hydrogen-terminated silicon surface at wafer scale. *Applied Physics Letters*, 78(3):309–311, 2001.

[19] J. Wagner. *Mikroskopie und Strukturierung von Materialoberflächen.* Lecture notes, TU Graz, 2009.

[20] B. Wei, N. Kobayashi, M. Ichikawa, T. Koyama, Y. Taniguchi, and T. Fukuda. Organic solid laser pumped by an organic light-emitting diode. *Optics Express*, 14(20):9436–9443, 2006.

[21] C. Weißmantel and C. Hamann. *Grundlagen der Festkörperphysik.* Springer, 1980.

[22] L. Windholz. *Experimentalphysik 4.* Lecture notes, TU Graz, 2004.

[23] W. Xie, F. Li, H. Wang, Z. Xie, F. Shen, Y. Ma, W. Lu, D. Zhang, and D. Ma. Stimulated

emission from distyrylbenzene derivative crystals grown by vapor deposition. *Applied Optics*, 46(20):4431–4433, 2007.

[24] T. Yamao, K. Yamamoto, Y. Taniguchi, T. Miki, and S. Hotta. Laser oscillation in a highly anisotropic organic crystal with a refractive index of 4.0. *Journal of Applied Physics*, 103(9):093115, 2008.

[25] K. Yamashita, A. Arimatsu, N. Takeuchi, M. Takayama, K. Oe, and H. Yanagi. Multi-layered solid-state organic laser for simultaneous multiwavelength oscillations. *Applied Physics Letters*, 93(23):233303, 2008.

[26] K. Yamashita, A. Kitanobou, M. Ito, E. Fukuzawa, and K. Oe. Solid-state organic laser using self-written active waveguide with in-line Fabry–Pérot cavity. *Applied Physics Letters*, 92(14):143305, 2008.

[27] Y. Yang, G. A. Turnbull, and I. D. W. Samuel. Hybrid optoelectronics: A polymer laser pumped by a nitride light-emitting diode. *Applied Physics Letters*, 92(16):163306, 2008.

# EIDESSTATTLICHE ERKLÄRUNG

Ich erkläre an Eides statt, dass ich die vorliegende Arbeit selbstständig verfasst, andere als die angegebenen Quellen/Hilfsmittel nicht benutzt, und die den benutzten Quellen wörtlich und inhaltlich entnommene Stellen als solche kenntlich gemacht habe.

Graz, am ……………………………            ……………………………………………………..
                                                                                (Unterschrift)

# STATUTORY DECLARATION

I declare that I have authored this thesis independently, that I have not used other than the declared sources / resources, and that I have explicitly marked all material which has been quoted either literally or by content from the used sources.

……………………………            ……………………………………………………..
        date                                                          (signature)